Jülich Center for Hadron Physics (JCHP)
Institut für Kernphysik (IKP)
COSY

Spin-filtering with PAX

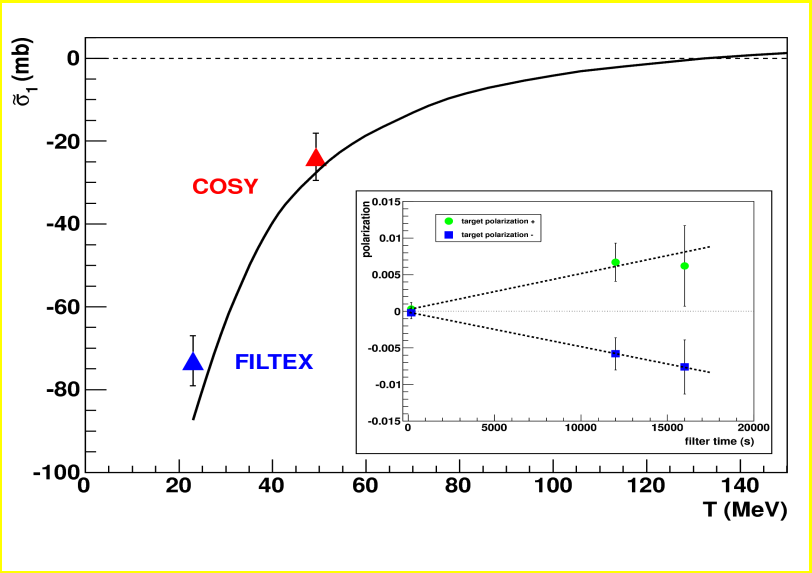

Annual Report 2012

Further Contributions

Mitglied der Helmholtz-Gemeinschaft

JÜLICH
FORSCHUNGSZENTRUM

K Further Contributions

1. Experimental Hadron Physics
   - 1.1 Measurements of $A_{x,x}$ and $A_{y,y}$ in the $np \to d\pi^0$ reaction at 353 MeV
   - 1.2 Luminosity Determination for the Quasi-free $pn \to pn\eta'$ Reaction
   - 1.3 Analysis of $\eta \to \pi^+\pi^-\gamma$ with WASA-at-COSY
   - 1.4 Search for $(^4\text{He-}\eta)_{\text{bound}}$ with WASA-at-COSY
   - 1.5 Calibration of the COSY-TOF Straw Tube Tracker
   - 1.6 Analysis of the $pp \to nK^+\sigma^+$ Reaction from COSY-TOF Data
   - 1.7 Analysis of a Feasibility Study of the Reaction $pn \to pK^0\Lambda$
   - 1.8 Transverse Spin Filtering at COSY — Final Results
   - 1.9 Polarization in proton deuteron breakup at 50 MeV
   - 1.10 Measurement of the nuclear polarization in H_2 and D_2 molecules after recombination of polarized hydrogen or deuterium atoms
   - 1.11 Energy Calibration For The WASA-at-COSY Forward Detector
2. Theoretical Physics (see Sect. B [of Annual Report] for links to published papers)
3. Accelerator Division
   - 3.1 Radiation Protection
   - 3.2 Calculation of electron motion in the toroid of the 2 MeV cooler at COSY
4. Preparations for FAIR
   - 4.1 Design Simulations for Pellet Tracking Systems
   - 4.2 Development of a Readout and Test System for the Forward Strip Part of the Micro Vertex Detector of PANDA
   - 4.3 Development of Front End Electronics for the PANDA Straw Tube Tracker (STT)
   - 4.4 Upgrade of the Jülich Digital Readout System for the PANDA-MVD
   - 4.5 Implementing an Ethernet Communication Module Based on the UDP Standard into the Jülich Digital Readout System
   - 4.6 Implementations of Hough Transformations on GPUs for PANDA
   - 4.7 Si Detector Test for the HESR Day-One Experiment
   - 4.8 Towards the Data Transmission from PandaRoot to the Compute Node
   - 4.9 Time Resolution of a Flash-ADC System for the PANDA STT

Measurements of $A_{x,x}$ and $A_{y,y}$ in the $np \to d\pi^0$ reaction at 353 MeV*

V. Shmakova[1,2] and S. Dymov[2,3]
for the ANKE collaboration

The ANKE beam time in May-June 2011 was designed for the measurement of the transverse spin correlation $A_{x,x}$ in the $\vec{n}\vec{p} \to \{pp\}_s\pi^-$ reaction at 353 MeV [1]. However, as by-products from this double polarized experiment we could also investigate the spin-correlation coefficients $A_{x,x}$ and $A_{y,y}$ in the $\vec{n}\vec{p} \to d\pi^0$ reaction. In the experiment a vector polarized deuteron beam with kinetic energy 706 MeV interacted with an internal polarized hydrogen target. The $\vec{n}\vec{p} \to d\pi^0$ production was then studied in quasi-free kinematics using the data obtained on the $\vec{d}\vec{p} \to d\pi^0 p_{\rm sp}$ reaction.

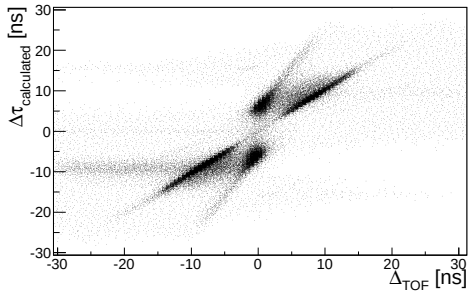

Fig. 1: Measured time of flight (TOF) difference for two particles $\Delta_{\rm TOF}$ versus the one calculated under assumption that the detected particles were a proton and deuteron ($\Delta\tau$).

The final deuteron and the (fast) spectator proton $p_{\rm sp}$ were detected in the ANKE Forward Detector (FD). The pd pairs were identified by the differences in their times of flight (TOF) [2]. Figure 1 shows the measured TOF difference plotted versus the TOF calculated under assumption that the detected particles were a proton and deuteron. Genuine pd-pairs are therefore to be found along the diagonal in this plot. Events corresponding to the $dp \to d\pi^0 p_{\rm sp}$ reaction were selected from the pion peak in the missing-mass spectrum.

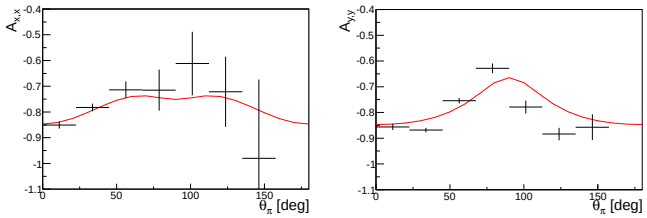

Fig. 2: The values of $A_{x,x}$ (left panel) and $A_{y,y}$ (right panel) measured in the $np \to d\pi^0$ at 353 MeV as a function of the pion polar angle θ_π. The results are compared with the SAID predictions [3].

In order to extract values of $A_{x,x}$ and $A_{y,y}$, the experimental asymmetry was expressed in the form:

$$\xi = \frac{\Sigma_1 - \Sigma_2}{\Sigma_1 + \Sigma_2} = PQ(A_{x,x}\sin^2\phi_\pi + A_{y,y}\cos^2\phi_\pi), \qquad (1)$$

where ϕ_π is the azimuthal angle of the pion in the laboratory reference frame. The values of the beam and target polarization ($P = 0.69$ and $Q = 0.5$) were those obtained in an earlier analysis and we neglect the small P_z and Q_z components that may arise in a quasi-free measurement due to the Fermi motion in the deuteron. Here $\Sigma_1 = N_{\uparrow\uparrow} + N_{\downarrow\downarrow}$ and $\Sigma_2 = N_{\uparrow\downarrow} + N_{\downarrow\uparrow}$, where $N_{\uparrow\uparrow}$ etc. are the numbers of events with the beam and target spin directed as indicated by the arrows.
After evaluating the values of ξ/PQ for each pion c.m. polar angle θ_π bin, a linear fit in $\cos^2\phi_\pi$ allowed the $A_{x,x}$ and $A_{y,y}$ coefficients to be extracted on the basis of Eq. (1).

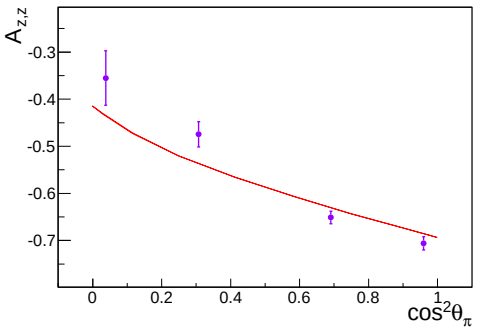

Fig. 3: $A_{z,z}$ measured in the $np \to d\pi^0$ reaction at 353 MeV as a function of $cos^2\theta_\pi$ compared with the SAID predictions [3].

The results obtained for $A_{x,x}$ and $A_{y,y}$ are compared in Fig. 2 with the SAID predictions [3] for the isospin-related $\vec{p}\vec{p} \to d\pi^+$ reaction. Due to the fitting process, the measurements of $A_{x,x}$ and $A_{y,y}$ are strongly correlated. This is far less the case for $A_{z,z} = 1 + A_{x,x} + A_{y,y}$, which is largely independent of $A_{x,x} - A_{y,y}$. The fluctuations in this observable shown in Fig. 3 are therefore smaller.

References:

[1] S. Dymov *et al.*, COSY proposal #205 (2011), http://collaborations.fz-juelich.de/ikp/anke/proposals.shtml
[2] S. Dymov *et al.*, Phys. Rev. C 81, 044001 (2010).
[3] SAID data base, http://gwdac.phys.gwu.edu.

[1] IKP, Forschungzentrum Jülich, 52425 Jülich, Germany
[2] LNP, JINR, 141980 Dubna, Russia
[3] Phys. Inst. II, Universität Erlangen-Nürnberg, 91058 Erlangen, Germany

* Supported by the COSY-FFE program.

Luminosity Determination for the Quasi-free $pn \to pn\eta'$ Reaction

J. Klaja[1] for the COSY-11 collaboration

The COSY–11 collaboration has measured the excitation function of the $pn \to d\eta'$ reaction [1] using a deuteron target and a proton beam of 3.365 GeV/c momentum. Simultaneously to that investigation, the $pn \to pn\eta'$ reaction has been measured. These data are competitive to the dedicated $pn \to pn\eta'$ study performed at 3.35 GeV/c [2] from which an upper limit for the cross section could be extracted. Due to the higher beam momentum an increased count rate is expected, thus finite in a cross section value. The first step of the analysis is the determination of the time integrated luminosity.

The determination of the luminosity is based on the registration of the quasi-free $pp \to pp$ reaction [3].

A sketch of the experimental setup is shown in Fig 1.

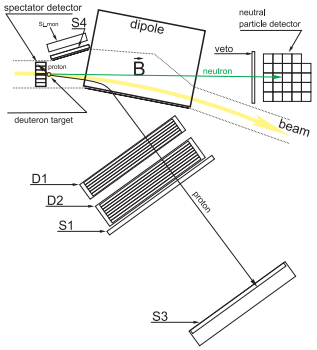

Fig. 1: Scheme of the COSY–11 detector system with superimposed tracks from the $pd \to p_{spec}(pn\eta')$ reaction. D1 and D2 denote the drift chambers. S1, S3, S4 and veto stand for the scintillation detectors. The neutral particle detector is used for the neutron registration. Si_{mon} and spectator detector are silicon strip detectors to detect elastically scattered protons and spectator protons, respectively.

The quasi-free proton-proton scattering was measured in parallel to the η' meson production in proton-neutron collisions. In these reactions, the beam proton interacts with the proton bound inside the deuteron target. The recoil proton is measured by the scintillator S4 and by the position sensitive silicon detector Si_{mon} (see Fig 1). The forward proton is bent in the magnetic field of the dipole towards the drift chambers and scintillator detector. The details concerning the detection setup can be found in [2, 4]. The momentum of the fast proton is determined by tracking back the trajectory reconstructed from signals in the drift chambers.

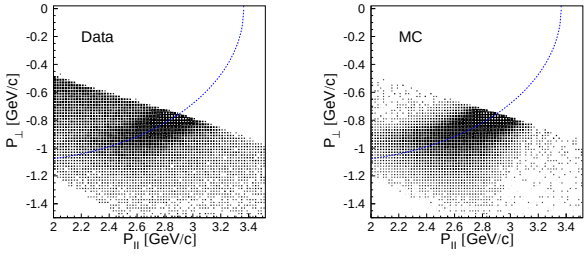

Fig. 2: Parallel versus transversal momentum component of the reconstructed forward proton momentum as obtained in the experiment **(left)** and in the simulation **(right)**.

Figure 2 shows the parallel versus transversal component of the reconstucted momentum of the forward scattered proton. Events corresponding to the elastic scattered protons are located near the kinematical ellipse marked as a solid line. To determine the luminosity, the known differential cross section for elastically scattered protons is compared to the count rate of scattered protons from the experimental data. However, for quasi–free elastic scattering we have to deal with Fermi motion of the nucleons inside the deuteron. This motion implies that the value of the total energy in the center-of-mass system as well as the direction of the center-of-mass velocity varies from event to event. This means that in a single subrange of scattering angle in the laboratory system there are events originating from scattering at different values of the total energy s, as well as different scattering angles in the proton-proton center-of-mass system. Therefore in order to calculate the time integrated luminosity we have to perform simulations taking into account these effects. Each simulated event is associated with a weight corresponding to the differential cross section which is a function of the scattering angle and the total energy in the center-of-mass system $\sqrt{s}$. For this purpose we have used the cross section values for the $pp \to pp$ reaction computed by means of the SAID programme [5] because the accessible data base of the EDDA collaboration was insufficient. In our case, the effective beam momentum which is seen from the nucleon inside the deuteron changes from 2.2 GeV/c up to 4.5 GeV/c whereas EDDA measurements were performed in the range of beam momenta from 0.712 GeV/c to 3.387 GeV/c.

In order to calculate the integrated luminosity, we have divided the available range of the S1 detector into four subranges. For each subrange, the distance of each event from the kinematical ellipse was determined, the background was subtracted from the distance distribution and the real number of scattered events $\Delta N_{exp}(\theta_{lab})$ was obtained. The result for one subrange is shown in Fig 3 (left).

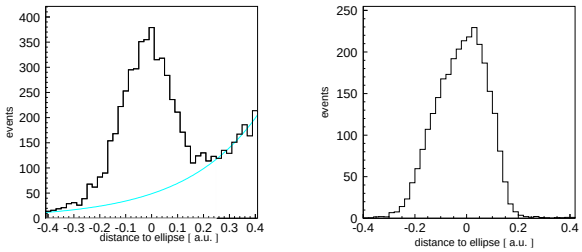

Fig. 3: **(left):** Distribution of the distances from the expected kinematical ellipse for the experimental data. **(right):** Distance distribution of the simulated data.

In order to determine $\Delta N_{MC}(\theta_{lab})$, we have simulated $N_0 = 10^7$ quasi-free $pp \to pp$ events, which have been analysed using the same procedure as for the experimental data. The result for the corresponding subrange as for the experimental distribution is shown in Fig 3 (right). Assuming, that N_0 is the total number of simulated events, the integrated luminosity is given by: [3]:

$$L = \frac{N_0}{2\pi} \frac{\Delta N_{exp}(\theta_{lab})}{\Delta N_{MC}(\theta_{lab})}.$$

We have determined the integral luminosity for all subranges of the S1 detector individually and subsequently the average value. The average integrated luminosity is equal to $L = (2.34 \pm 0.05) x 10^{36} cm^{-2}$.

The overall systematic error of the integrated luminosity is estimated to be 8%. The main source for the systematic error is the background subtraction. For the evaluation of this systematic uncertainty, the background was subtracted in two ways, namely in one case the background was described by an exponential function, in the other case a linear background was assumed. The difference between the two methods is considered as systematic error resulting in a value of $\pm 6\%$.
As a next step in the analysis of the $pn \to pn\eta'$ reaction, the detection efficiency of the COSY-11 system will be estimated and the missing mass calculated.

References:

[1] P. Moskal et al., COSY Proposal **No. 155** (2005).
[2] J. Klaja et al., Phys. Rev. **C81**, 035209 (2010).
[3] P. Moskal, R. Czyżykiewicz, AIP Conf.Proc. **950**, 118 (2007).
[4] J. Klaja Ph.D. thesis, Jagiellonian University, (2009), e-Print: arXiv:0909.4399
[5] The CNS Data Analysis Center, http://www.gwu.edu

[1] M. Smoluchowski Institute of Physics, Jagellonian University, Cracow, PL-30-059 Poland

Analysis of $\eta \to \pi^+\pi^-\gamma$ with WASA-at-COSY

D. Lersch

The decay $\eta \to \pi^+\pi^-\gamma$ is suitable to study QCD anomalies at the chiral limit, since this decay is driven by the box anomaly [1]. However measurements have shown, that a correct description of this decay can only be achieved by including final state interactions. The experimental observables to test interaction models are:
i) The relative branching ratio: $\frac{\Gamma(\eta\to\pi^+\pi^-\gamma)}{\Gamma(\eta\to\pi^+\pi^-\pi^0)}$
ii) The photon energy E_γ distribution
In order to measure both quantities in one experiment, the reaction $pp \to pp[\eta \to \pi^+\pi^-\gamma]$ has been investigated. The data have been acquired during spring 2010 and 2012 using the WASA-at-COSY facility [2].

The recent analysis focusses on reconstructing $\eta \to \pi^+\pi^-\gamma$-events, but also investigates the channel $\eta \to \pi^+\pi^-\pi^0$. This channel is important for determining the relative branching ratio.

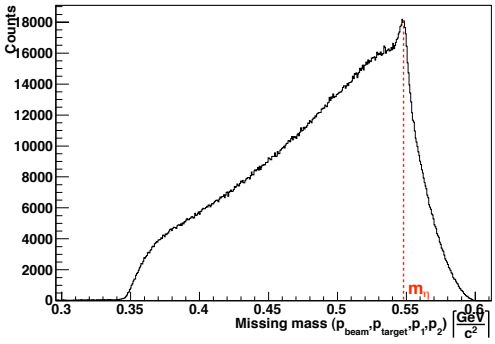

Fig. 1: Missing mass distribution deduced from the initial state and the two final state protons. The red linie indicates the η-mass at $0.548\,\mathrm{GeV/c^2}$.

Figure 1 shows the two proton missing mass spectrum after particle identification in the forward detector of WASA. A peak at the η-mass is visible, on top of a large background from direct pion production. In order to reduce that background and select $\eta \to \pi^+\pi^-\gamma$ events, a least squares kinematic fit with constraint on energy and momentum conservation has been used. Events with a fit probability larger than 10% are accepted. In addition to that criterion, events with small photon energies and small opening angles between charged and neutral particles have been rejected (see Figure 2). Pions cause hadronic split-offs in the calorimeter, which are reconstructed as low energy photons. $\eta \to \pi^+\pi^-\pi^0$-events are alos selected by using a kinematic fit too with the same constraints as mentione above plus the additional constraint $\pi^0 \to \gamma\gamma$. 1.2% of the 2010 data set has been analysed with this analysis chain and the preliminary results for both analyses are shown in Figure 3. In both cases the background has been determined by using an iterative peak clipping algorithm (SNIP). 703 $\eta \to \pi^+\pi^-\gamma$ and 1,500 $\eta \to \pi^+\pi^-\pi^0$ -events have been reconstructed. In a next step, the relative branching ratio will be calculated (which requires the reconstruction efficiencies of both channels) and the photon energy E_γ distribution for $\eta \to \pi^+\pi^-\gamma$ will be determined.

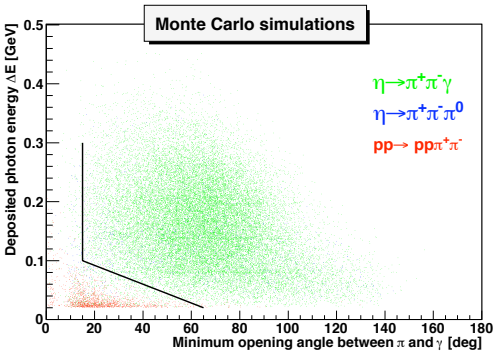

Fig. 2: Plot of the photon energy as a function of the minimum opening angle between charged pions and photons. This plot is obtained for Monte Carlo simulations. The black line indicates the cut, which is used to reject split-off events. Events above and to the right of that line are accepted.

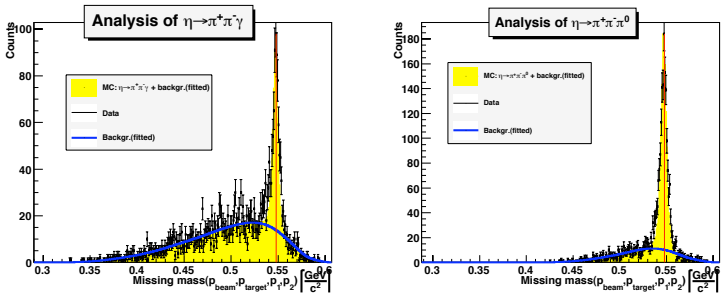

Fig. 3: Left: missing mass distribution deduced from two protons for the analysis of $\eta \to \pi^+\pi^-\gamma$. Right: missing mass distribution deduced from two protons for the analysis of $\eta \to \pi^+\pi^-\pi^0$

References:

[1] Wess, Zumino, *Phys. Lett*, **B37**,95,(1971), Witten, *Nucl. Phys.*,**B223**,422,(1983)
[2] H.-H Adam et al., Proposal for the wide angle shower apparatus (WASA) at COSY-Jülich, (200)4

Search for $(^4\text{He-}\eta)_{bound}$ with WASA-at-COSY

W. Krzemien[a], P. Moskal[a] and M. Skurzok[a] for the WASA-at-COSY collaboration

We carried out a search for the ^{4}He-η bound state by measuring the excitation function for the $dd \to {}^3\text{He}p\pi^-$ and $dd \to {}^3\text{He}n\pi^0 \to {}^3\text{He}n\gamma\gamma$ reactions at energies in the vicinity of the η production threshold.
In 2008 an exclusive measurement of the excitation function for the $dd \to {}^3\text{He}p\pi^-$ reaction was performed. The data were taken during a slow acceleration of the beam from 2.185 GeV/c to 2.400 GeV/c crossing the kinematic threshold for the η meson production in the $dd \to {}^4\text{He}\,\eta$ reaction at 2.336 GeV/c. The integrated luminosity in the experiment was determined using the $dd \to {}^3\text{He}n$ reaction. The shape of the excitation function for the $dd \to {}^3\text{He}p\pi^-$ reaction was examined. No signal from η-mesic ^{4}He was observed. An upper limit for the cross-section for the bound state formation and decay in the process $dd \to (^4\text{He-}\eta)_{bound} \to {}^3\text{He}p\pi^-$ was determined to the 90 % confidence level and it varies from 20 nb to 27 nb as the width of the bound state varies from 5 MeV to 35 MeV. The upper limits depend mainly on the width of the bound state and only slightly on the binding energy.

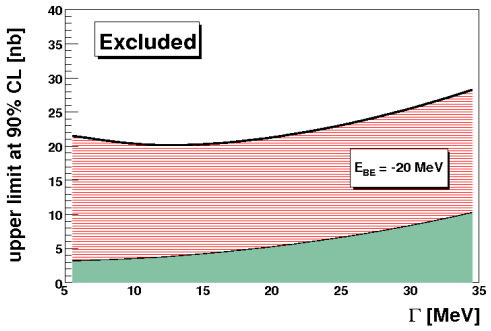

Fig. 1: Upper limit at the 90 % confidence level of the cross-section for formation of the $^4\text{He}-\eta$ bound state and its decay via the $dd \to (^4\text{He-}\eta)_{bound} \to {}^3\text{He}p\pi^-$ reaction as a function of the width of the bound state. The binding energy was set to E_{BE}=-20 MeV. The green area at the bottom represents the systematic uncertainties.

For the first time in the experimental search for mesic nuclei all ejectiles were measured and the reaction was identified exclusively. The results of this analysis have been accepted for publication in Phys. Rev. C [2].
In November 2010 a factor 30 higher statistics was collected compared to the 2008 measurement. Until now the $dd \to (^4\text{He-}\eta)_{bound} \to {}^3\text{He}n\pi^0 \to {}^3\text{He}n\gamma\gamma$ reaction was analysed. The ^{3}He was identified in the Forward Detector based on the ΔE-E method. The neutral pion π^0 was reconstructed in the Central Detector from the invariant mass of two gamma quanta originating from its decay while the neutron four-momentum was calculated using the missing mass technique.
The excitation function for the $dd \to {}^3\text{He}n\pi^0 \to {}^3\text{He}n\gamma\gamma$ reaction is determined for the "signal-rich" region corresponding to the momenta of the ^{3}He in the CM system below 0.3 GeV/c and the "signal-poor" region for the ^{3}He CM momenta above 0.3 GeV/c. The cut applied is indicated by the blue line in Fig. 2.

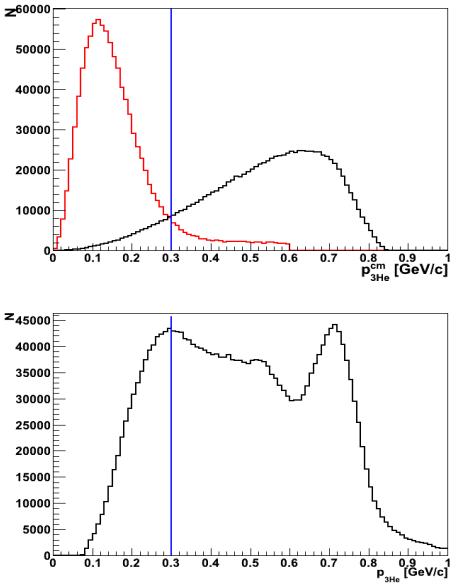

Fig. 2: (Upper plot) Distribution of generated the ^{3}He momentum in the CM for Monte Carlo simulations for $dd \to (^4\text{He-}\eta)_{bound} \to {}^3\text{He}n\pi^0 \to {}^3\text{He}n\gamma\gamma$ (red line) and for the phase-space $dd \to {}^3\text{He}n\pi^0 \to {}^3\text{He}n\gamma\gamma$ (black line). (Lower plot) The distribution of ^{3}He in the CM system measured in the experiment. The blue line in both plots marks the cut applied to separeate "signal-rich" and "signal-poor" regions.

The simulation was done for the beam momentum range $p_{beam} \in (2.127, 2.422)$ GeV/c. The shape of the background and relative contribution of various reaction channels is under investigation.

Additional selection criteria such as cut in the opening angle between neutron an π^0 in CM frame or cut in θ_{3He} in LAB will be applied to investigate the shape of the excitation functions.
The luminosity is determined based on the $dd \to {}^3\text{He}n$ reaction. The ^{3}He is selected via a cut on the Edep(FRH1) vs Edep(FRH2) spectrum (Fig. 3 left panel). In the next step of the analysis, helium stopped in FRH3 or in FRH4 (Fig. 3 left panel) is taken into account.
The number of $dd \to {}^3\text{He}n$ events is determined from the missing mass spectrum. To reject three and four-body reactions we take into account only events which gives no more than one neutral cluster in the Central Detector. Monte Carlo simulations show that using of this condition reject only about 6% of $dd \to {}^3\text{He}n$ events. Therefore it allows to considerably reduce the background without significant loss of signal counts. The analysis and studies of systematics of applied cuts are in progress. Luminosity will be determined as a function of $cos\theta_{cm}$ and the excess energy Q.

We acknowledge support by the Foundation for Polish Science - MPD program, by the Polish National Science

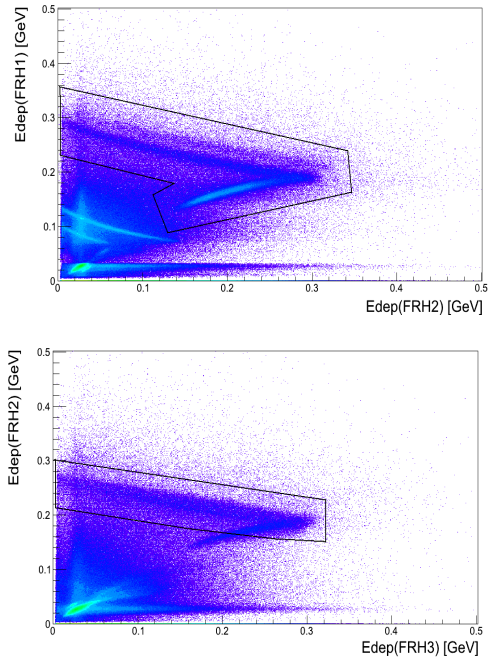

Fig. 3: Cuts in Edep(FRH1) vs Edep(FRH2) spectrum (upper panel) as well as in Edep(FRH2) vs Edep(FRH3) (lower panel) applied for helium identification in $dd \rightarrow {}^{3}\mathrm{He}n$ reactions.

Center through grant No. 2011/01/B/ST2/00431 and by the FFE grants of the Research Center Juelich.

References:

[1] W. Krzemień, *PhD Thesis, Jagiellonian Univ.* (2011)
[2] P. Adlarson, *et al., arXiv:1301.0843* (2013)

[a] M. Smoluchowski Institute of Physics, Jagiellonian University, 30-059 Cracow, Poland

Calibration of the COSY-TOF Straw Tube Tracker

Sedigheh Jowzaee[a] for the COSY-TOF collaboration

The Straw-Tube-Tracker (STT) is an essential detector in the COSY-TOF experiment which provides accurate position information of charged particle tracks. Therefore, a precise calibration of the STT is important to reduce errors in the track reconstruction and to increase the reconstruction efficiency and spatial resolution. Hence, pp elastic scattering events measured in Fall 2012 at 2.95 GeV/c beam momentum are analyzed for calibration of the STT. The main goal is the deduction of the correlation between measured drift times or TDC values and the isochrone radii which are the track to wire distances. At first some corrections were done on each single straw TDC spectrum including:

- Selection of first hit;
- Signal width cut;
- Electronics offset correction.

A charged track ionizes molecules by passing the straw tube gas. Several ionization clusters are created along this track and can be recorded when using fast shaping electronics, but the main timing information is contained in the cluster which is closest to the wire and which has the minimum drift time. Figure 1 (left) shows the raw TDC spectrum which includes all hits and noise. To remove the multiple hits the TDC times related to leading and trailing edges are sorted and the first one was taken for calibration. In Figure 1 the effect of the multiple hits removal is shown on the right.

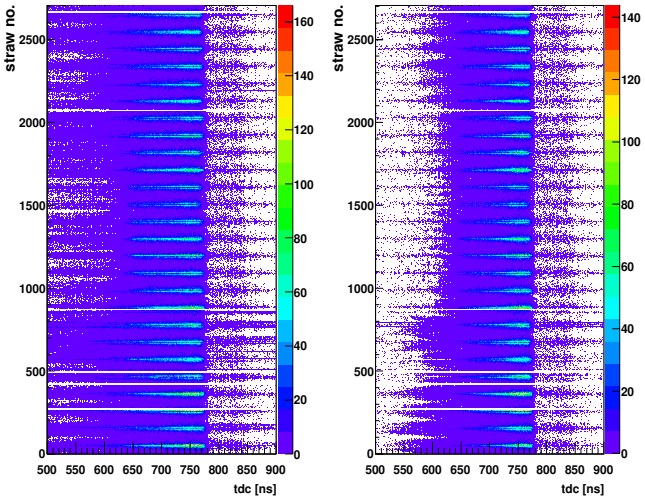

Fig. 1: (Left) TDC spectrum without correction for $5 \cdot 10^6$ hits in the 2704 single straw tubes. The horizontal white lines are related to empty single straw spectra. Using the common-stop readout of the TDCs, higher values correspond to shorter drift times. (Right) TDC spectrum per single straw tubes after removing multiple hits. The plot only shows the 1^{st} leading edge time of the signals.

The TDC spectrum for single straws after removing multiple hits still shows some noisy channels in the straws 770 and 790 and were not removed completely by the first cut. In order to remove the remaining noise hits, the width between the leading and following trailing edge times was considered. The electronics readout gives a minimum limit of 5 ns width and it is a type of limit on the pulse height. Moreover, only noise or unreal events which have a small pulse height consist of a leading time without the following trailing time. They can produce a width lower than 5 ns limit, so the width spectrum was cut for less than this limit. The width cut removes most of the noisy hits from the TDC spectrum as shown in Figure 2.

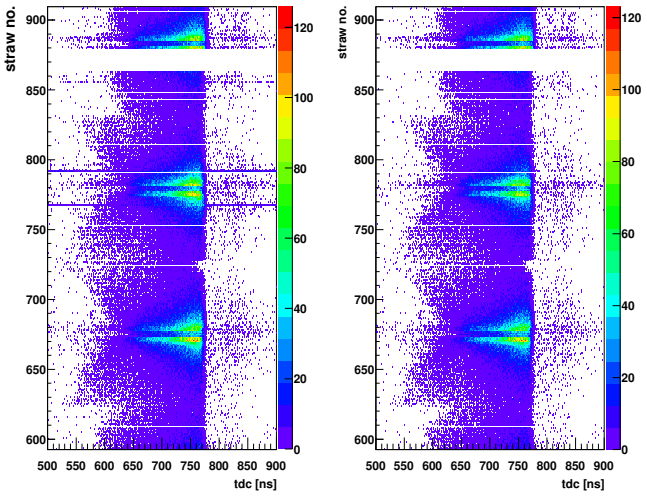

Fig. 2: (Left) TDC spectrum before the signal width cut, the effect of noise is seen in the straws 770 and 790. (Right) TDC spectrum per single straw after a cut on the signal width. The cut value is 5 ns.

After removing multiple hits and applying the width cut, the spectra were analyzed for electronics offset correction. The irregular shape of the maximum edge in the TDC spectrum (Fig.3 left) is largely because of electronics offset related to different readout modules. Each group of 16 straws has the same readout electronics board. For correction of the electronics offset an error function was fitted to the leading edge of the TDC spectra for each single straw. A reference point was defined as the sum of the turning point of the fit function and one sigma. This reference point was corrected to an arbitrary time (780 ns) for each single straw. The offset corrected maximum edge of TDC spectrum is shown on the right in Figure 3.

The main point of calibration is the determination of the correlation between the drift time and the isochrone radius. For this aim, the corrected TDC or time distribution was divided into 130 bins of 1 ns width each in the time window 650-780 ns and for each of bins the isochrone radius was calculated using the formula,

$$r(t_i) = \int_{t_0}^{t_i} v_{drift}(t)\,\mathrm{d}t = R\frac{\sum N_i}{N_{tot}} \qquad (1)$$

where t_0 is the starting point of the spectrum equal to the largest drift time, R is the difference between the straw tube radius and the wire radius, N_i is the number of tracks in the t_0 to t_i interval. This method which is called the "Self calibrating" method [1, 2] requires homogenous illumination in the whole straws. Figure 4 shows the calibration curve between

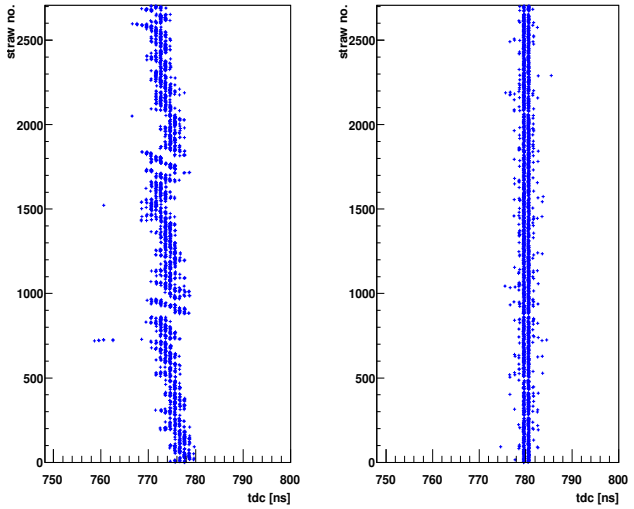

Fig. 3: (Left) Maximum edge of TDC spectrum per single straw. The irregular shape is predominantly a result of electronics offset from different boards of the readout system. (Right) TDC spectra after corrected for each single straw offset.

the drift time and the isochrone radius for all double layers. A double layer consists of 208 straw tubes.

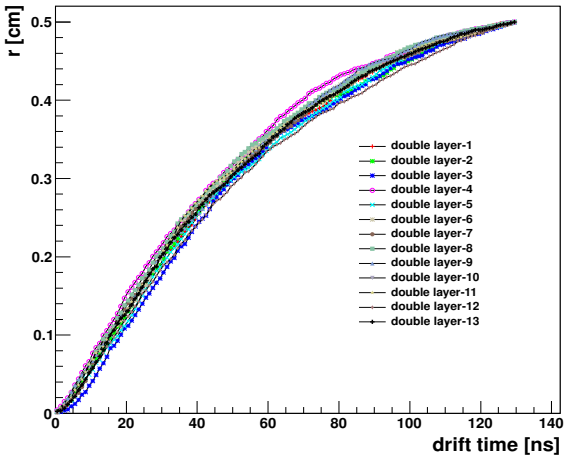

Fig. 4: Isochrone radius to drift time curve for 13 double layers.

Using these calibration curves the track reconstruction will be done to improve the drift time to isochrone radius calibration. Furthermore, the calibration curve will be redone with the reconstructed tracks which give distance to the wire information. Afterwards, correction of the propagation time through the straw wire and calibration of the straw position will be performed and the spatial resolution of the straws will be determined.

We acknowledge support by the Foundation for Polish Science - MPD program, co-financed by the European Union within the European Regional Development Fund and by the FFE grants of the Research Center Jüelich.

References:

[1] R. Dzhygadlo, PhD Dissertation, University of Bonn, 2012.

[2] M. Röder, PhD Dissertation, University of Bochum, 2011.

[a] Jagiellonian University, Krakow, Poland

Analysis of the $pp \to nK^+\Sigma^+$ Reaction from COSY-TOF Data

Paweł Klaja[a] for the COSY-TOF Collaboration

A high statistics measurement with the newly upgraded setup in August 2010 was dedicated to hyperon production with a polarized proton beam of 2.95 GeV/c momentum. The main goal of this experiment was to measure the spin triplet component of the $p\Lambda$ scattering length, the spin transfer coefficient of the $pp \to pK^+\Lambda$ reaction and the investigation of N^* resonances. In addition, the $pp \to nK^+\Sigma^+$ reaction was registered at an excess energy of Q = 128.7 MeV.

The upgrade at the COSY-TOF detector setup was a new tracking system which consists of the Straw Tube Tracker (STT) and the Silicon Quirl Telescope (SQT). The silicon quirl telescope was mounted 2.57 cm from the target. This allows for a direct measurement of Σ^+ hyperons ($c\tau = 2.404$ cm).

First, events with two charged tracks reconstructed by the STT were selected. One of the tracks having additional hits in the Start detector and SQT was assumed to be a kaon and the other one without any other conditions was treated as a decay particle (π^+ or proton from Σ^+ decay). Additionally, one hit in the calorimeter with no corresponding Quirl or Ring detectors hit (neutron), and one reconstructed pixel in the SQT detector not belonging to the K^+ and the decay track was demanded. At this stage of the analysis the full geometrical information about the primary particles as well as the decay track was obtained.

The plane constructed by the decay track vector and the assumed target point was calculated. The point where the kaon track vector crosses that plane was used in the further analysis as the primary interaction point and the reconstructed Σ^+ and neutron tracks were refited to that point. Based on the geometrical information about the reconstructed primary tracks (n_n, n_{K^+}, n_{Σ^+} unit vectors), the absolute values of their 3-momenta were determined with the following formula :

$$p_{beam} = p_n \cdot n_n + p_{K^+} \cdot n_{K^+} + p_{\Sigma^+} \cdot n_{\Sigma^+}. \qquad (1)$$

Next, geometrical cuts determined using Monte Carlo simulations were applied. The topology of the reaction allows for maximal polar angles of 40° and 20° for the kaon and Σ^+, respectively. In principle it is possible to measure the full polar angle range of those particles but due to combinatorial background the cuts on maximal angels for kaon and Σ^+ were applied. On the other hand the measurement is mostly limited by the acceptance of calorimeter, which only allows neutrons below 12 ° to be registered.

The next step was to check whether the neutrons from Σ^+ decay were not misidentified as primary neutrons. The decay particles must lay in the same plane with the Σ^+. One can calculate the coplanarity within the system of the decay:

$$coplanarity = \angle(\Sigma^+, n) + \angle(\Sigma^+, \pi^+) - \angle(n, \pi^+). \qquad (2)$$

Coplanarity equal to zero means that all particles are in the same plane and the measured neutron could be a secondary one, that is why for the further analysis only events with coplanarity greater than zero will be utilized.

Afterwards, the geometrical constraint which is the z-coordinate of the Σ^+ decay vertex was checked. This was calculated as the point of closest approach between the Σ^+ track and the decay charged track. The position of this point in the beam direction must be located between the SQT and STT.

Next, the difference between velocities calculated from the time-of-flight measurement (β_{TOF}) and the geometry measurement (β_{geom}) was checked for the kaon track. According to resolution only events with differences $|\beta_{TOF} - \beta_{geom}| < 0.5$ were selected.

The last signature used in the analysis was the kink angle between the Σ^+ and the decay track. This geometrical constraint as a function of decay particle velocity allowed to select between the two main decay branches of the Σ^+. This dependence is presented in Figure 1. One can see a clear separation between the two decay channels for the Monte Carlo sample. Selecting $\Sigma^+ \to n\pi^+$ eliminates half of the events but gets rid of main background channel $pp \to np\pi^+$ reaction, from which protons or pions could be misidentified as a decay of Σ^+ at small angles.

The missing mass of the K^+n system was calculated for the resulting sample and is shown in Figure 2.

10^7 $pp \to nK^+\Sigma^+$ events were simulated assuming realistic experiment conditions. The sample was analyzed using the same conditions as in the analysis of real data. The reconstruction efficiency was determined to be on the order of 1.5×10^{-3}.

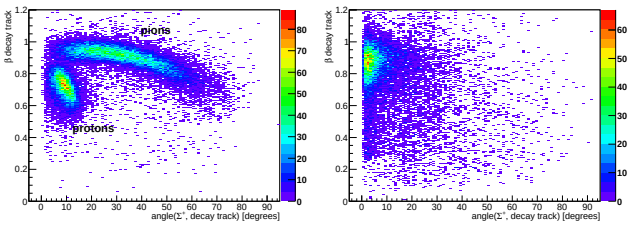

Fig. 1: Angle between Σ^+ and decay tracks as a function of decay particle velocity, left panel Monte Carlo, right panel data, respectively. One observes clear separation of decay channels $\Sigma^+ \to n\pi^+$ and $\Sigma^+ \to p\pi^0$ in the left panel according to β and angle.

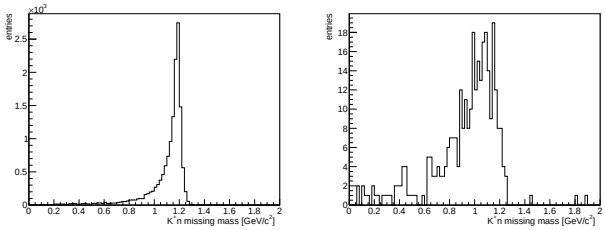

Fig. 2: Missing mass distribution of the K^+n system for Monte Carlo (left) and data (right).

The selection criteria used in the analysis of simulation and data were set to have as high efficiency as possible, and must be verified using background channels simulations.

Studies of background channels in order to determine the number of $pp \to nK^+\Sigma^+$ reaction events are in progress.

[a] Physikalisches Institut, Friedrich-Alexander-Universität Erlangen-Nürnberg, 91058 Erlangen, Germany

Analysis of a Feasibility Study of the Reaction pn $\rightarrow$ pK$^0\Lambda$

E. Roderburg for the COSY-TOF collaboration

1 Introduction

First measurements of the Λ production on the neutron were done with the old setup of the COSY-TOF detector, they are documented in [1]. The new setup with the Straw Detector is especially suited for detection of secondary vertices and therefore test data with a deuterium target were taken in November 2011 in order to examine the feasibility of the measurement of pn $\rightarrow$ p$K^0\Lambda$. The momentum of the polarized proton beam was 2.7 GeV/c. The trigger was set to more than or equal than four tracks in the stop counters and at least one track in the start counters. The experimental setup of the COSY-TOF detector with the Straw Tube Tracker is described in detail in [2].

2 Method of Analysis

The first step of the analysis is to select events with five tracks, one track emerging from the target region and two pairs of tracks arising from secondary vertices. As an example for such an event, hits in one of three orientations of the Straw Tube Tracker shown in Fig. 1.

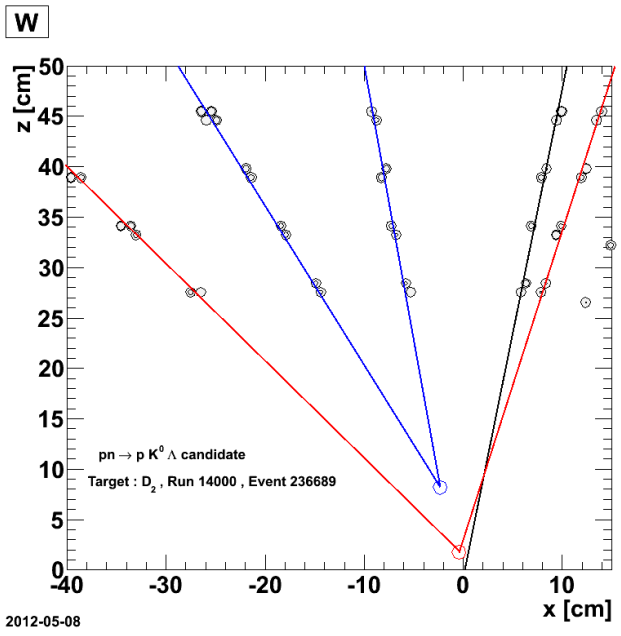

Fig. 1: p$K^0\Lambda$ signature measured with the Straw Tube Tracker. The outer circles show the straw tube circumference, the inner ones represent the circle obtained by the drift time information, this circle is tangential to the track.

The decay vertex positions of the Λ and the K^0 are fit based on the information of the corresponding two tracks. The primary vertex position is calculated as the intersection of the proton track with the line, which results from the intersection of the decay planes of the Λ and the K^0. With these calculations all particle directions are known. The event selection criteria taken from the geometry are given in the following table:

primary vertex	z $<$ 10 mm
primary vertex in x,y plane	r $<$ 5 mm
secondary vertices	z $>$ 15 mm
closest approach of vertex tracks	$<$ 5 mm
proton scattering angle	$<$ 26 degrees
K^0 scattering angle	$<$ 44 degrees
Λ scattering angle	$<$ 22 degrees

The absolute momenta of the Λ and the K^0 are determined by their direction and the directions of their decay particles. Assuming the particle masses and applying energy and momentum conservation between the initial state (beam + neutron) and final state, the three components of the Fermi momentum (P$_f$) and the absolute value of the primary proton (P$_p$) momentum can be calculated.

For each event the calculation is done twice a) with the hypothesis that the first vertex is the K^0 and the second vertex the Λ and b) with reversed assignments. If both assumptions produce a solution for the equation system, the solution with the lower Fermi momentum is chosen.

In order to reduce the background from wrongly interpreted event signatures, events with reconstructed Fermi momenta larger than 300 MeV/c are rejected.

3 Reconstruction Efficiency and Resolution

The combined acceptance and reconstruction efficiency is determined with a Monte Carlo program to be 2.3% for pn $\rightarrow$ pK$^0\Lambda$ at the beam momentum of 2.7 GeV/c, including the fact, that only K^0_s are detected. (This value has to be compared with the combined acceptance and reconstruction efficiency of pp $\rightarrow$ pK$^+\Lambda$, which is about 8-9%.)

The resolution for the different observables are determined from the differences of the Monte Carlo start values and the reconstructed values, they are given in the following table:

Kaon momentum:	σ (P$_K$)/P$_K$	=	1.4 %
Λ momentum:	σ (P$_\Lambda$)/P$_\Lambda$	=	10 %
Proton momentum:	σ (P$_P$)/P$_P$	=	10 %
squared invariant pΛ mass:	σ (m$^2_{p\Lambda}$)/m$^2_{p\Lambda}$	=	1.6 %

4 Results

The data sample was collected during about 3 days where the intensity of COSY was about $5 \cdot 10^6$ protons. 450 events of pn $\rightarrow$ pK$^0\Lambda$ with the criteria given above are extracted from these data.

The Fermi momentum is reconstructed on an event by event basis, the comparison between data and reconstructed Monte Carlo data is shown in Fig. 2, where a good agreement is observed.

The distribution of the distances of the secondary vertices to the target is an important quality check for the data, it is seen in Fig. 3 by the comparison between reconstructed Monte Carlo data without background, and the data that the background is low and that the assignment of the vertices to K^0 and Λ is working very well.

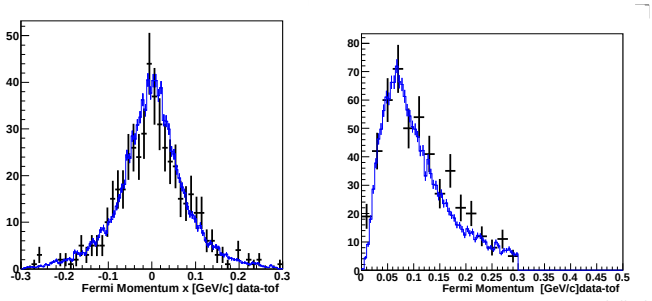

Fig. 2: Comparison of the Fermi momentum calculated from Monte Carlo Input (blue line) with the Fermi momentum deduced from the data (black). Left: x component of the Fermi momentum, right: absolute value of the Fermi momentum.

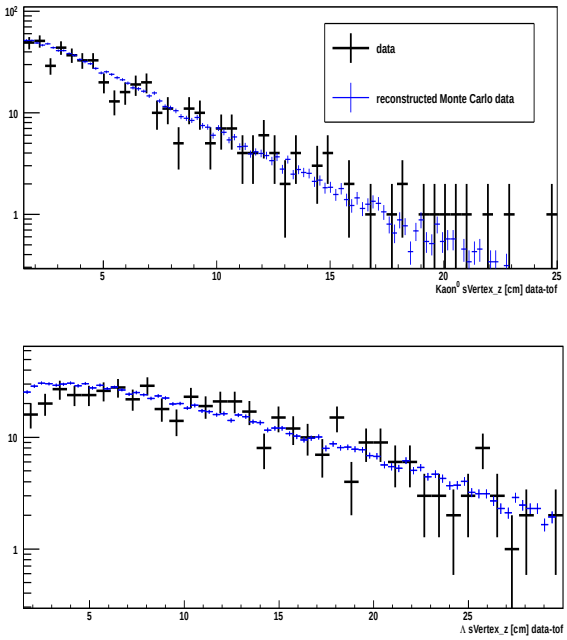

Fig. 3: z - distance distribution of the vertices assigned to the K^0 (upper figure) and to the Λ particle (lower figure).

The angular distributions are shown in Fig. 4. The reconstruction efficiency combined with the acceptance is shown for each angular distribution by the blue histogram. For backward K^0 the yield drops strongly, as the decay pions have larger angles due to the smaller forward boost. Deviations from the forward - backward symmetry due to the Fermi motion and due to the mass difference of proton and neutron are negligible.

5 Discussion

The angular distributions of $\cos(\vartheta)^{cm}$ of the Kaon and the Λ do not show significant deviations from anisotropy, while the distribution of the proton shows an indication for the presence of higher partial waves. Compared to the reaction pp $\rightarrow$ p K^+ Λ [3],[4] the sign of the curvature of the proton angular distribution is opposite to the one of the reaction pn $\rightarrow$ p K^0 Λ. For a precise determination of the coefficients of Legendre polynomials data with higher statistics is needed.

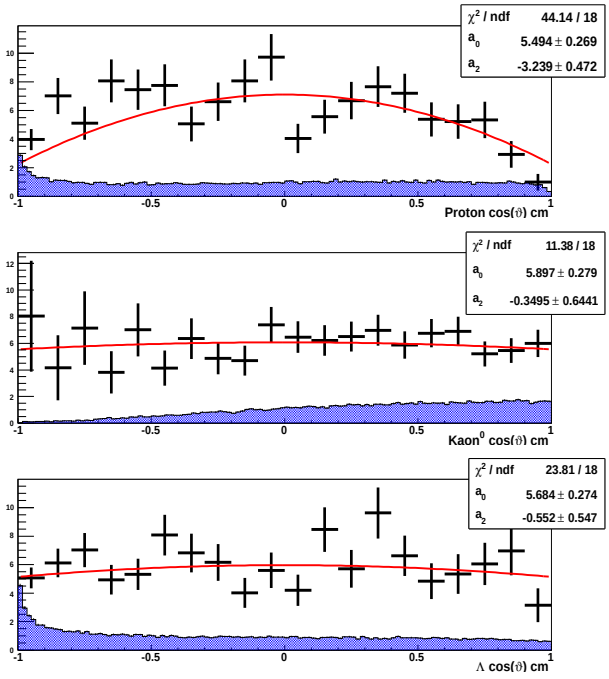

Fig. 4: Angular distributions in the center of mass system: top: proton, center: Kaon, bottom: Λ. The red line shows a fit with the function $a_0 + \frac{1}{2}a_2(3cos\vartheta^2 - 1)$. The distributions are acceptance corrected. The acceptance as a function of the polar angle is given in each figure by the blue area.

References:

[1] M. Krapp, Ph. D. Thesis, University of Erlangen-Nuernberg (2012).
[2] M. Roeder, Ph. D. Thesis, University of Bochum (2012).
[3] M. Fritsch, Thesis University of Erlangen-Nuernberg (2002) page 84.
[4] COSY-TOF collaboration, Eur. Phys. J. A. **46** (2010) 27.

Transverse Spin Filtering at COSY - Final Results

PAX collaboration

The PAX-Collaboration[1] is investigating spin dependent attenuation as a method to produce polarized antiproton beams. In 1993 this method has been shown to work with protons at the FILTEX in Heidelberg. During spin filtering a stored beam suffers spin dependent attenuation by multiple traversal of a polarized internal gas target. More particles of one state than the other are scattered out of the ring acceptance and a polarized beam remains.

Experimental Setup In autumn 2011, a spin filtering experiment was performed at Jülich-COSY using a stored proton beam at $T_p = 49.3\,\mathrm{MeV}$ (see Fig. 1).

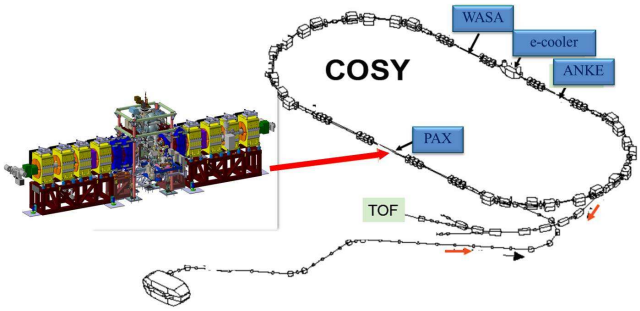

Fig. 1: The PAX-setup inside the COSY-ring.

The polarized target and its polarimeter performed smoothly during the whole data taking period. The density in the target cell was measured through the observed beam deceleration induced by the target gas, and detected by the Schottky signal yielding a value of $(5.5 \pm 0.2) \cdot 10^{13}$ atoms/cm^2 for one injected hyperfine state from the atomic beam source. The target polarization was continuously monitored by the Breit-Rabi polarimeter and the Target Gas Analyzer, and the total target polarization was found to be $Q_y = 0.73 \pm 0.05$ and constant in time. The magnetic field coils mounted at the chamber provided the vertical weak holding field ($B \approx 10\,\mathrm{G}$), required to define the quantization axis for the target polarization.

The polarization lifetime of the COSY beam was measured prior to the spin-filtering experiments to be $(2.0 \cdot 10^5 \pm 5 \cdot 10^4)\,\mathrm{s}$, confirming the prediction that no depolarizing resonances are present in the neighbourhood of the chosen machine tunes. In view of the polarization build-up experiment, the beam polarization lifetime can be considered as infinite. In order to reduce systematic errors, spin-flips of the beam polarization have been introduced at every measurement cycle. The spin-flipper employs a resonant RF-solenoid and is part of the standard equipment of the COSY ring. Before the measurement, the spin-flipper has been tuned to the proper working conditions and its efficiency has been measured in dedicated runs to be $\varepsilon_{SF} = 0.989 \pm 0.001$.

The beam polarization has been measured by means of the polarimeter installed at the ANKE interaction point in the opposite straight section of COSY (see Fig. 1). Beam polarimetry has been accomplished by making use of the analyzing power in proton-deuteron elastic scattering. For this purpose, two three-layer silicon detectors have been employed to detect the elastically scattered particles in the interaction between the stored proton beam and the ANKE deuterium cluster target. The telescopes were symmetrically placed with respect to the target and longitudinally positioned in order to optimize the figure of merit (FOM $= \frac{d\sigma}{d\Omega}(\theta) \cdot A_y^2(\theta)$) of the reaction. The energy of the experiment has been chosen to be 49.3 MeV, at this energy a precise determination of the beam polarization is possible, because accurate analyzing power data are available. Elastically scattered deuterons and protons were clearly identified by the deposited energy in the different layers. Due to the low energy of the reaction, there was no background for deuterons, while some (small) background for protons came from deuteron breakup.

Spin-filtering measurements The sequence of operations in a spin-filtering cycle is as follows (see Fig. 2):

- The unpolarized proton beam is injected in the COSY ring at 45 MeV. The beam is cooled and accelerated to an energy of 49.3 MeV for the measurement. The typical number of particles injected and accelerated for every cycle was $(5 \ldots 12) \cdot 10^9$;
- At this point the spin-filtering cycle starts. Polarized gas is injected into the storage cell at the PAX interaction point and the holding field coils are powered. The typical duration of a spin-filtering cycle was two beam lifetimes, corresponding to a total spin-filtering time of 16000 s.
- At the end of the spin-filtering period, the PAX polarized target was switched off, and the ANKE deuterium cluster target and the data acquisition of the beam polarimeter were started. During the beam polarization measurement the beam polarization has been reversed twice by using the spin-flipper. This allows the determination of the induced beam polarization for every cycle, thereby reducing systematic errors. The total duration of a polarization build-up cycle was 18500 s;
- Spin-filtering cycles have been repeated for different directions of the target holding fields.

In order to provide a zero polarization calibration of the detector, a series of cycles without spin-filtering has been carried out. These cycles reflected exactly the same sequence of

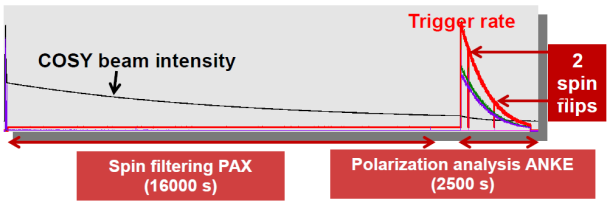

Fig. 2: Picture taken from an online monitor of the COSY control room representing a spin-filtering cycle. At the end of the cycle the trigger rate can be noticed together with the two points in time where the spin flipper was activated.

[1] **P**olarized **A**ntiproton e**X**periments

operations, differing only in the number of injected particles ($< 1 \cdot 10^9$) and the duration of the spin-filtering part, which was reduced from 16000 s to 180 s in the zero calibration measurements.

Data analysis The effective polarizing cross section can be derived from the measurement of the rate of polarization buildup in the stored beam:

$$\tilde{\sigma_1} = \frac{dP}{dt}\frac{1}{Qd_t f}\,. \tag{1}$$

The beam polarization is measured by using $p^{\uparrow}d$ elastic scattering. The cross section for the interaction of a transversely polarized proton beam impinging on an unpolarized deuterium target is given by

$$\frac{d\sigma}{d\Omega}(\theta,\phi) = \frac{d\sigma_0}{d\Omega}[1 + PA_y(\theta)\cos\phi]\,, \tag{2}$$

where $d\sigma_0/d\Omega$ is the unpolarized cross section, $A_y(\theta)$ is the analyzing power, θ is the polar and ϕ the azimuthal scattering angle in the laboratory system.

Deuterons and protons stopped in the second or third detector layer can be clearly identified by means of the $\Delta E/E$ method. Since the data were taken below the pion-production threshold, an identified deuteron ensures that elastic scattering took place. In order to distinguish elastically scattered protons from the ones that stem from deuteron breakup, a cut based on the relation between deposited energy and scattering angle has been applied. The contamination of the selected elastic proton sample from protons originating from pd-breakup events is estimated to be less than 3%. The presented analysis is based on a total number of $8.6 \cdot 10^6$ identified deuterons and $1.6 \cdot 10^6$ identified protons.

The beam polarization P is derived from the asymmetry determined using the so-called cross ratio-method. It provides a cancellation of all first order false asymmetries caused by differences in acceptance, efficiency, and integrated luminosity in the two detectors. The cross ratio δ is defined by means of the rates $Y_{R,L,\uparrow,\downarrow}$ detected in the left (L) and right (R) detectors for data samples with spin up ($\uparrow$) and down ($\downarrow$) beam polarizations,

$$\delta = \sqrt{\frac{Y_{L,\uparrow}(\theta,\phi)\cdot Y_{R,\downarrow}(\theta,\phi)}{Y_{L,\downarrow}(\theta,\phi)\cdot Y_{R,\uparrow}(\theta,\phi)}} = \frac{1+PA_y(\theta)}{1-PA_y(\theta)}\,. \tag{3}$$

In Eq. 2, the average of the trigonometric function accounting for the azimuthal dependence of the analyzing power over the detector acceptance in the interval $25^\circ < \phi < 25^\circ$ has been approximated to unity without affecting the measured asymmetry. The selected events are sorted in bins of 3° width. The polarization is extracted by scaling the measured asymmetry using a fit based on a 5th order polynomial of the analyzing power taken from N.S.P. King et al. (Phys. Lett. B, 69 (1977), p. 2). In order to investigate fake asymmetries as possible sources of systematic errors, the same analysis procedure has been applied to the zero measurements, where no spin-filtering took place and no polarization was induced in the beam.

The beam polarization obtained from spin-filtering cycles of different length for the two target spin-orientations is presented in Fig. 3. The plot presents the total acquired statistics including events where either a deuteron or a proton from elastic scattering were identified. A linear fit to the five points shown in Fig. 3 allows us to determine $\frac{dP}{dt} = (4.8 \pm 0.8) \cdot 10^{-7}\mathrm{s}^{-1}$

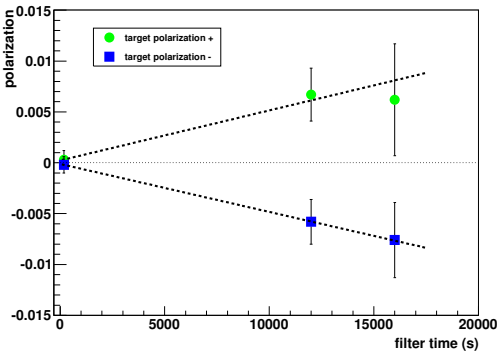

Fig. 3: Polarization induced in the beam after filtering for different times and different signs of the target polarization during spin filtering.

Results and Conclusions By substituting the results of the previous Section in Eq. (1), together with the revolution frequency f of 510032 Hz in the ring at the experiment energy of $T_p = 49.3$ MeV, we finally obtain:

$$\sigma_1^{\tilde{meas.}} = -23.5^{\pm 3.9(\mathrm{stat.})}_{\pm 1.9(\mathrm{syst.})}\ \mathrm{mb}. \tag{4}$$

The measured cross section can be compared to the predicted one, based on the present knowledge of the pp spin-dependent interaction as given in the SAID data base $\sigma_1^{\tilde{theo.}} = -26.9$ mb (Fig. 4).

The PAX Collaboration has successfully completed a spin-filtering experiment using a beam of protons at COSY. The measurement allowed us to extract the polarizing cross-section in proton-proton interactions and represents a milestone in the field. It confirms that spin-filtering can be effectively used to polarize a stored beam in situ and that our understanding of the mechanism in terms of the proton-proton interaction is correct: the predictions are in excellent agreement with the available data. The achievement is of fundamental importance in view of the possible application of the method to polarize a beam of stored antiprotons.

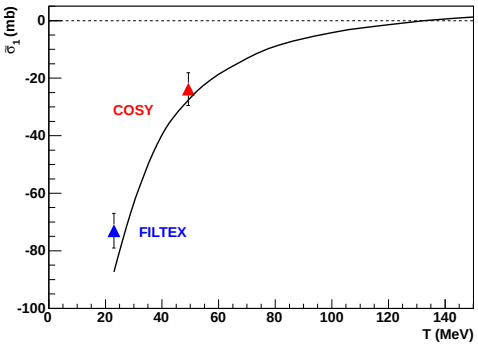

Fig. 4: Measured spin-dependent polarizing cross section for the interaction (only statistical errors are shown). The solid line represents the prediction from the SAID database.

Polarization in proton deuteron breakup at 50 MeV

Z. Bagdasarian, S. Bertelli, D. Chiladze, A. Kacharava, P. Lenisa, N. Lomidze, G. Macharashvili, K. Marcks von Würtemberg, F. Rathmann, M. Tabidze, P. Thörngren Engblom and M. Zhabitsky

A complete doubly polarized proton deuteron breakup experiment measuring most of the 22 spin observables at low energy with large acceptance is planned to be done at COSY. The main objectives for the study are twofold; to provide a testing ground for the modern theory of nuclear forces, the chiral effective field theory, and to study the effects of three-nucleon interactions in a conclusive way within this framework. Additional significant motivation worthwhile special attention is the fact that the proton deuteron breakup scattering process constitutes both the background and an obvious potential source of symmetry breaking observables in foreseen experimental tests of fundamental symmetries such as TRIC.

A precursor *pd* breakup experiment was done in 2011 using a vertically polarized proton beam at 49.3 MeV and the deuterium cluster-jet target at the ANKE facility. The ANKE Silicon Tracking Telescopes (STTs) placed to the right and to the left of the target measured the four-vectors of the two outgoing protons. The two STTs comprised three double-sided segmented detectors of 69 μm, 300 μm and 5 mm thicknesses.

For the determination of the beam polarization the $\overrightarrow{p}d$ elastic channel was recorded concurrently with the breakup. The shape of the angular distribution of the deuteron was compared to previously measured data. The $\overrightarrow{p}d$ breakup reactions are identified by calculating the neutron missing mass given the energy losses and the directions of the two detected protons, see Fig. 1. A total number of breakup events of the order of 10^6 is expected to be reconstructed from the available data taking into account the acceptance and track reconstruction efficiency obtained by an analysis of simulated events using GEANT4.

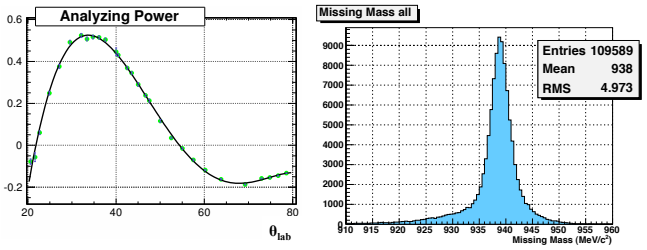

Fig. 1: *Left*: A_y from *pd* elastic scattering data taken for the determination of the beam polarization resulting in $P_{beam} = 0.738 \pm 0.002$ (statistical uncertainty). *Right*: The missing mass including all event hit patterns using a preliminary energy calibration.

The analysis is in progress using an improved relative and absolute calibration scheme that is being developed. In Fig. 2 the stability of the correction multipliers deduced grouped according the electronic chip readout pattern are shown accomplishing alignment of the energy loss in the segments.

Theoretical predictions according chiral effective field theory In search of interesting areas of phase space and to guide the final analysis of $A_y(breakup)$ the

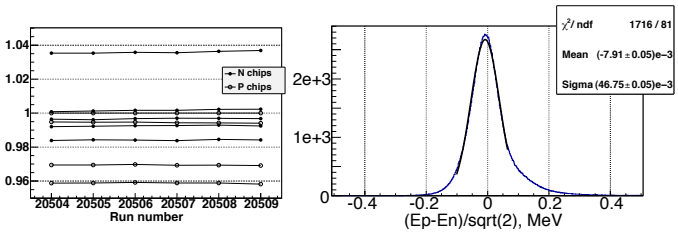

Fig. 2: *Left*: The relative correction multipliers for the energy loss in segments connected to the same electronic chips are shown versus run nos. 20504-20509 of the Aug11 PAX experiment. The example here concerns a 300 μm layer. The filled (empty) dots represent the n-side (p-side) of the detector. *Right*: The difference between the energy deposited as measured by the n- and p-sides after the correction factors were implemented.

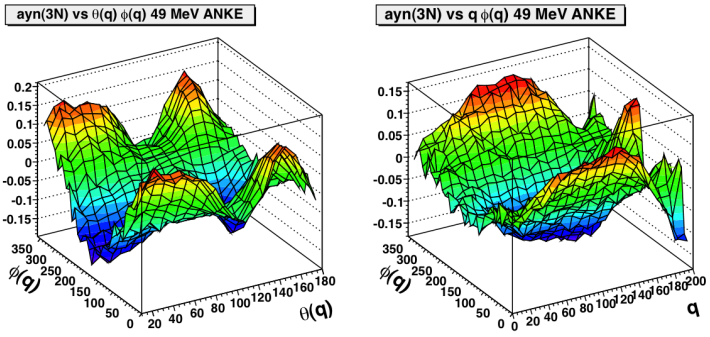

Fig. 3: Theoretical predictions according N2LO including 3NFs for Ay as function of the neutron center-of-mass momentum q retrieved using the sampling method and an isotropic simulation of *pd* breakup for the overall geometry of the Aug11 experiment ($\phi_{protons} = [-30, 30]$ and $\theta_{protons} = [40, 115]$ deg).

sampling method was applied to an isotropically simulated event sample with only geometrical cuts using multidimensional linear interpolation on a grid of precalculated theoretical values[1]. In Fig. 3 theoretical predictions according N2LO (using cutoff $\Lambda = 550$ MeV) including three-nucleon interactions are shown. As an example here A_y is displayed as function of the neutron center-of-mass momentum q, its polar (θ_q) and azimuthal ϕ_q angles.

The present data will yield results concerning the nucleon vector analyzing power of $\overrightarrow{p}d$ breakup in comparison to the theoretical approach at third and fourth order of chiral effective field theory. A spin-off of the analysis is that once $A_y(breakup)$ is determined for the present detection setup this observable can be applied as an alternative way to extract the beam polarization obtained through spin filtering of an unpolarized proton beam[2].

[1] The theoretical grids were created by A. Nogga.

[2] The spin filtering was done in $p\overrightarrow{p}$ and the resulting beam polarization was measured by $\overrightarrow{p}d$ reactions.

Measurement of the nuclear polarization in H_2 and D_2 molecules after recombination of polarized hydrogen or deuterium atoms

R. Engels, R. Gorski[a], K. Grigoryev[a,b], L. Kotchenda[b], P. Kravtsov[b], M. Mikirtychyants[a,b], F. Rathmann, H. Paetz gen. Schieck[c], H. Seyfarth, H. Ströher, S. Terekhin, V. Trofimov[b], N. Chernov [b], and A. Vasilyev[b]

When polarized hydrogen atoms recombine in a storage cell, the residual H_2 molecules may still show nuclear polarization [1]. In a collaboration between PNPI, University of Cologne, and FZ Jülich a device was built in the framework of an ISTC project (No. 1861) and a DFG project (436 RUS 113/977/0-1) to measure the polarization of hydrogen (deuterium) atoms and hydrogen (deuterium) molecules after recombination of polarized atoms depending on different surface materials, temperatures and magnetic fields.

When the polarized atomic beam source (ABS) of the ANKE experiment is not in use at COSY, investigations of the interaction of polarized atoms with the surface of a T-shaped storage cell inside a superconducting solenoid were carried out. In the actual measurements the polarized hydrogen atoms can recombine on a gold surface at temperatures between 40 and 120 K. Afterwards, both particles, atoms and molecules are ionized by an electron beam passing this cell. The protons and H_2^+ ions produced are accelerated and send into a Lamb-shift polarimeter (LSP) [2].

With some minor modifications of the existing Wienfilter, the first component of the LSP, both ion species are well separated due to the different velocities at the same energy (see Fig. 1). From the measured currents for both ions it was obvious that the recombination on the gold surface was at least 95%. More precise values are difficult to obtain, because the average free path of the H_2^+ ions at the pressures in the storage cell ($\sim 10^{-4}$ mbar) is less than the cell length (400 mm) and, therefore, some of these ions are lost. This effect decreases the intensity of the H_2^+ ions and the measured recombination rate.

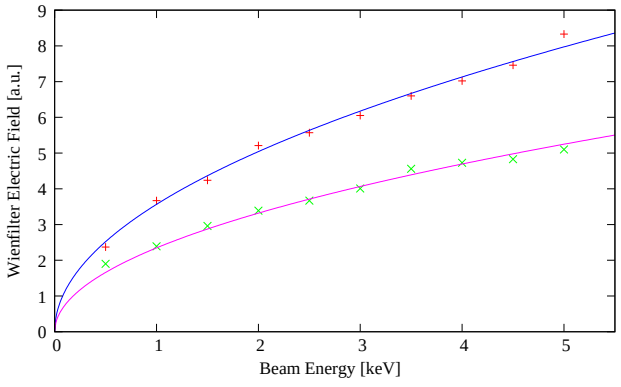

Fig. 1: When the magnetic field of the Wienfilter is set to a fixed value, e.g. to 18 mT, the protons and H_2^+ ions can be filtered out at different energies.

Parallel to the production of protons by ionizing hydrogen atoms it is even possible to produce protons from H_2 molecules. Only the cross section is smaller by a factor of about 7. For the case of large recombination it is obvious, that most of the protons stem from the molecules and just a few from the atoms. Therefore, we tried to investigate the polarization of the molecules by the measurement of the proton polarization as a function of the magnetic field along the cell with the LSP (see Fig.2).

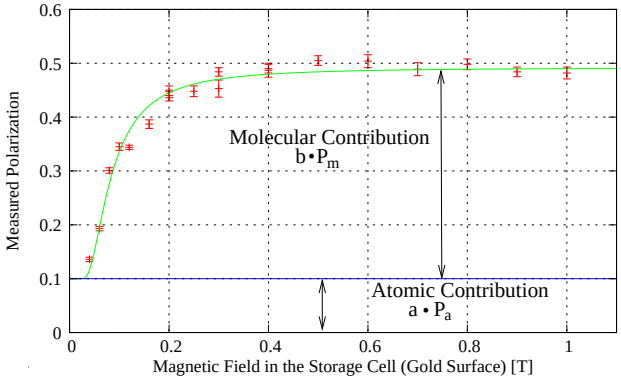

Fig. 2: Measured polarization of the outcoming protons as a function of the magnetic field in the storage cell (zemperature: 44 K), when the recombination inside the cell is very large. The fraction a are protons produced from hydrogen atoms and b protons stem from the molecules.

For the large recombination shown before one can assume that the polarization of the atoms in the cell is equal to the polarization $P_a = 0.88$ of the ABS atomic beam itself, because the atoms cannot had have many depolarizing wall collisions before recombination. With a constant atomic contribution of $a \cdot P_a = 0.1$ to the measured polarization the fraction of protons from atoms must be $a = 11.4\%$ and, therefore, $b = 88.6\%$. Than, the nuclear polarization in the molecules is $P_m = 0.442 \pm 0.006 = 1/2P_a$. This agrees with a naive model that recombination at these pressures will take place only on the gold surface and the atom, sitting on the gold surface, will be depolarized very fast. Thus, the recombined molecule will conserve the polarization of the incoming atom only. With use of Ref. [1] one can calculate in addition that the average amount of wall collisions in the cell is about 120 ± 10 which corresponds perfectly to the value from a simulation of 116. This leads to a measured recombination rate of $\sim 100\%$ of the hydrogen atoms on the gold surface, because the incoming flux of hydrogen atoms from the ABS beam is enough to set a to the measured value.

References:

[1] T.Wise et al., Phys. Rev. Lett. **87**, 042701 (2001).
[2] R. Engels et al., Rev. Sci. Instr. **74** (2003) 4607.

[a] Institut für Kernphysik, Forschungszentrum Jülich, Germany
[b] Petersburg Nuclear Physics Institute, Gatchina, Russia
[c] Institut für Kernphysik, Universität zu Köln, Germany

Energy Calibration For The WASA-at-COSY Forward Detector.

K. Demmich*, F. Bergmann*, P. Goslawski*, N. Hüsken*, F. Schepers* and A. Khoukaz*
for the WASA-at-COSY-Collaboration

One major subject of the WASA-at-COSY setup is the study of light mesons, which can be produced e.q. via the reaction p+d→ ^{3}He+X. By measuring the forward scattered ^{3}He nuclei the formed mesons can be identified by means of the missing mass method. This relies on an accurate calibration of the forward detector.
In October 2008 a test run for the reaction p+d→ ^{3}He+η' at an excess energy of 64 MeV has been carried out. In preparation of the analysis an accurate energy calibration has to be performed for the main energy detectors, the Forward Range Hodoscope (FRH) and the Forward Trigger Hodoscope (FTH), individually for every detector element. The energy loss ΔE is reconstructed based on the digitalised ADC value A delivered by the detector via

$$\Delta E \cdot \cos\vartheta = f_{\mathrm{NL}}\left(\frac{A\cdot\cos\vartheta}{f_{\mathrm{NU}}(\vartheta)}\right). \qquad (1)$$

The function f_{NU} corrects the polar angular dependent *non uniformity* of the detector and is parametrisized by a 3$^{\mathrm{rd}}$ order polynomial. In order to separate the non uniformity from energy depending effects, this function is fitted to the angular dependency of the ADC values of the minimum ionizing particles which have identical specific energy losses (Fig. 1).
After applying this first step the calibration function f_{NL} – again a 3$^{\mathrm{rd}}$ order polynomial – is determined, which corrects the energy depending *non linearity* of the detector. To avoid influences of the scattering angle, this second calibration is done for a narrow polar angle interval, e.g., $11° \leq \vartheta < 13°$. For the FRH the calibration parameters are determined by adjusting reconstructed to Monte Carlo simulated energy loss bands in the first three detector layers. The high complexity of this simultaneous fitting of three calibration functions requires a manual choice of start parameters, for which a graphical user interface has been developed (Fig. 2). Parameters can be varied easily and the effect can be monitored in real time. A further optimisation is achieved by the minuit fitting algorithm using an adjusted definition of χ^2 to handle the background the data set is afflicted with:

$$\chi^2 = \sum_{i=1}^{N} \min(\delta_i^2, \delta_{\mathrm{max}}^2).$$

Here N is the total number of data points, δ_i is the residual of the i-th data point divided by the uncertainty derived from simulations and δ_{max} is a constant limit defined before fitting.
Combining the non uniformity and the non linearity calibration for the full polar angular region of the forward detector the non uniformity parameters can be fine tuned by transferring the fitting algorithm from the non linearity calibration. This step completes the energy calibration.

*Institut für Kernphysik Westfälische Wilhelms-Universität, 48149 Münster, Germany

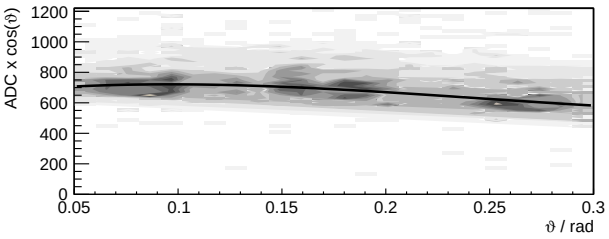

Figure 1: FRH: Angular dependence of ADC values for the MIPs and fitted non uniformity function.

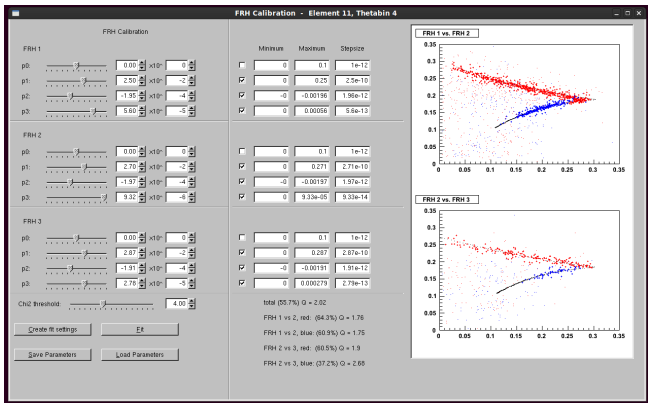

Figure 2: Graphical user interface for the FRH non linearity calibration.

A further energy loss detector is the FTH which is placed in front of the FRH. The energy reconstruction again follows equation (1). Hence, the non uniformity and the non linearity have to be determined with techniques adapted from the FRH calibration. The calibrated FRH energies allow for a direct comparison between calculated FTH energies (based on FRH energies) and measured ADC values. This dependency can be fittet by the non linearity function without any further user interactions.
This newly developed software package allows for a very accurate and fast calibration of the forward detector components. A detailled description can be found in [1].

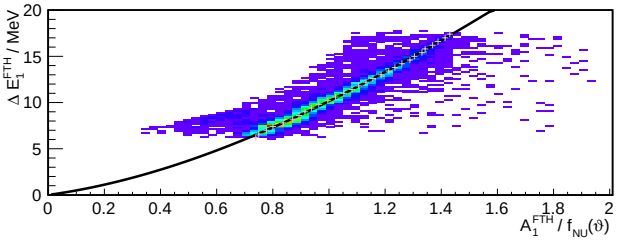

Figure 3: FTH: Calculated energy loss vs. measured ADC values and fitted non linearity function.

References

[1] K. Demmich, master thesis, 2013, Westfälische Wilhelms-Universität Münster

Radiation Protection

O.Felden, J.Göbbels, R.Hecker

Electronic personnel dosimetry

Since 2008 different types of electronic personnel dosimeter devices (EPD) and readout systems have been investigated at the IKP if they fulfill the requirements given at an accelerator facility. These EPDs, the succeeding models of the old-fashioned pencil dosimeters, are requested by the authorities due to the fact, that they are directly readable and have alerting functionality instead of the preferred DIS-1® electronic personnel dosimeter devices. In 2010/2011 we estabilised the discrepancy between the EPDs and the official film badges /DIS-1® Dosimeters in pulsed radiation fields with high doses. But the authorities still asked for the EPDs [3]. Because of the more suitable technical parameters of the MK2+® form Thermo Fisher Scientific this EPD will be the preferable dosimeter for use at COSY.
Driven by this demand we designed and built a new dosimeter station in the IKP-workshop and Electronic laboratory basing on the experience of the further readout systems. It is equipped with a panelPc running the readout software from Thermo Fisher scientific and a reading head communicating with the EPD-devices via IR.

Fig 1: At the dosimeter station (installation in the main building) the EPD with adapted alarm levels is assigned to the user.

This time the system was designed to fit the requirements of many institutes in the research center and therefore we installed a close collaboration with the central department for radiation protection (G-S) which is responsible for the data-storage and the institute for nuclear medicine (INM) as a second Institute interested in the use of pool-dosimeters. In the starting phase we built 6 dosimeter readout stations and set up five data managing stations and installed a redundant storage server system. Actually the database is hosted at the IKP while it is planned to move it to the central department for radiation protection. To improve the user friendliness and to reduce faults while entering the personal ID to the dosimeter system the readout stations were equipped with QR-Readers. As an alternative a RFID-Identifying system was developed and programmed by the IT-group of the IKP but it is not yet installed at the dosimeter stations.
Since mid of 2012 the system is running in productive mode and the average number of readouts is 140 /month in the IKP. The number is still increasing. Beside the colleagues (under radiation protection survey), guests or experimentalists working at COSY can use the dosimeters easily by entering special IDs directly by hand.

Dosimetry at the irradiation station at JULIC

The cyclotron JULIC obtains different possibilities to irradiate material or objects for different purposes. One irradiation station is inside the cyclotron vacuum chamber while the second station is located outside the vacuum system at the extracting beamline (fig. 2). Here we carry out irradiations of e.g. electronic devices or integrated circuits ICs to check the radiation hardness or whether they withstand cosmic radiation at satellites.

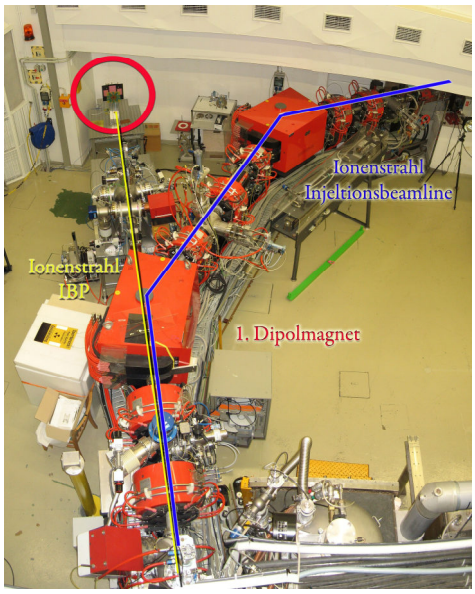

Fig 2: The picture shows the extraction beamline and the irradiation station (red circle) as seen from the top of the cyclotron JULIC

To obtain an equal irradiation of all objects and to measure the doses applied to the objects a measuring system with farmer ionization chambers TM30010® and a MULTIDOS®-Dosemeter from PTW is installed. To have more flexibility and measurement possibilities the readout system was enhanced [4]. A data-acquisition program basing on LabVIEW® form National Instruments was developed. It is now possible to use up to twelve ionization chambers but the number of chambers used can be changed easily. Bar-charts of the measured values of each chamber directly gives the customer the ratio of the dose rate applied to the components while a radar-plot shows if the shape and position of the beam fulfills the requirements given by the customer (fig. 3). Beside the dose measured on each chamber it is although possible to

have the averaged value over all ionization chambers. The measurements can be written down in protocol files while the measurement intervals can be varied starting from 500 milliseconds.

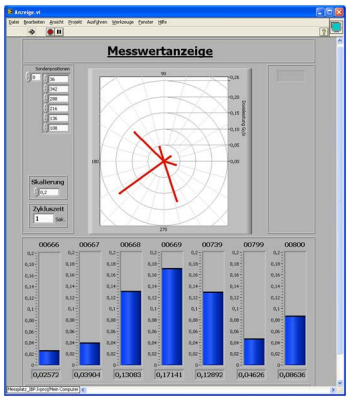

Fig 3: The Bar-charts show the difference in dose rate measured with the ionization chambers while the radar plot gives the beam shape relative to the mid-axis.

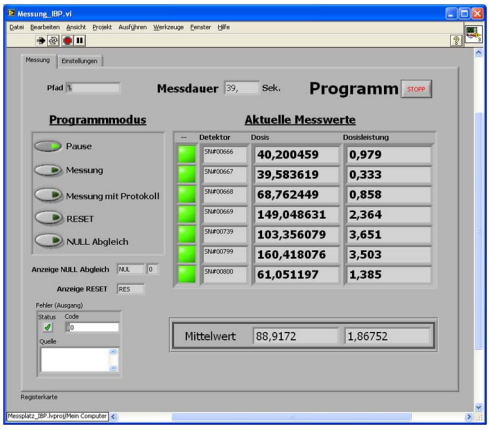

Fig 4: All measured values are displayed and in the last row the averaged dose applied to the object is shown.

In future it is planned to take other information, e.g. temperature, air pressure or humidity, although or to switch of the beam automatically if a given threshold is reached.

References:

[1] Strahlenschutzverordnung vom 20.07.2001
[2] Radiation Protection, IKP Annual report 2008
[3] Radiation Protection, IKP Annual report 2010
[4] Entwicklung eines Strahldiagnose-Vermessungssystem für online-Messungen zur Untersuchung der Strahlungs resistenz elektrischer Bauelemente. R.Hecker, diploma thesis 2012

Calculation of electron motion in the toroid of the 2 MeV cooler at COSY

L. Mao

The 2 MeV electron cooling device will be installed at COSY in order to boost the luminosity for future high density internal target experiments [1]. For effective electron cooling, strong magnetic field is required in the electron cooler to guide the electron beam. Both transport lines between the high voltage vessel and the cooling section consist of three 90° and one 45° toroids each. Due to the fringe magnetic field in a toroid section, the curvature radius has a variation at the transition from straight field section to bending toroid field section. Therefore the transverse velocity of electrons will increase after transition through the toroid. In this paper, a Runge-Kutta method was used to solve the electron motion equations in magnetic field. The variation of transverse velocity of electrons was calculated after transition through one 90° toroid. The result shows how the longitudinal magnetic field in toroid should be adjusted to avoid transverse velocity increase.

Considering an electron moving in an orthogonal curvilinear coordinate system related to a magnetic field only, the equation of electron motion is given by [2]:

$$\begin{aligned} \frac{d\vec{\mathbf{v}}}{dt} &= \vec{\mathbf{F}} = q\left(\vec{\mathbf{v}} \times \vec{\mathbf{B}}\right) \\ \frac{d\vec{\mathbf{r}}}{dt} &= \vec{\mathbf{v}} = V_s \cdot \hat{\mathbf{h}} + V_\perp \cos\theta \cdot \hat{\mathbf{n}} + V_\perp \sin\theta \cdot \hat{\mathbf{b}} \end{aligned} \tag{1}$$

Here the unit vector along the guide magnetic field is $\hat{h}$. The unit vector of the main normal of the force line and its binomial unit vector are $\hat{n}$ and $\hat{b}$, respectively. It is assumed that transverse velocity $V_\perp$ is much smaller than the velocity along the guide magnetic field V_s, and the longitudinal magnetic field was treated as a constant value. The approximate equations of the electron motion can be written as following [3]:

$$\begin{aligned} \frac{dV_\perp}{ds} &= V_\perp \frac{\partial \ln B}{\partial s}\frac{1}{2} - V_s K \cos\theta \\ \frac{d\theta}{ds} &= \left(\omega_H + V_s^2 K \sin\theta \frac{1}{V_\perp}\right)\frac{1}{V_s} \end{aligned} \tag{2}$$

Here K is the curvature vector of the force line. In order to include the fringe magnetic field in a toroid section, the curvature of 90° toroid was given by [4]:

$$K(s) = \frac{1}{4\rho}\left(\left(1+\tanh\left(\frac{s}{\Delta B}\right)\right)\left(1-\tanh\left(\frac{s-\pi\rho/2}{\Delta B}\right)\right)\right) \tag{3}$$

The factor ΔB described a variation at the transition from straight field to toroid field, ρ is the curvature radius. The fringe shape of K for a 90° toroid was shown in fig-1 with $\Delta B = 0.05$ and $\rho = 1.0$.

These ordinary differential equations can be solved with the Runge-Kutta method. Here a single electron motion in the 90° toroid was calculated. The electron energy is 2 MeV, the radius of toroid is 1.0 m. The calculation starts with the electron transverse velocity at 5×10^5 m/s and the phase values are 0, $\pi/2$, π, $3\pi/2$, respectively. The compensation of drift velocity in the toroid was not considered in calculation.

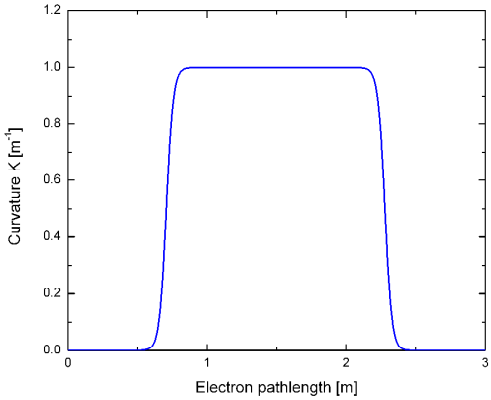

Fig. 1: Curvature of the electron beam trajectory in toroid. The bend starts at s=0.7 m.

Figure 2 shows the transverse velocity after transition through the toroid as a function of the longitudinal magnetic field. The length of the toroid is 1.57 m. It is clear that the minimum variation of the transverse velocity is observed when the length of the toroid is equal to integer number of the Larmor length. When the longitudinal magnetic field is high enough, the Larmor length is small and the kick of transverse motion is small, too. The worst case occurs when the toroid length is equal to half-integer Larmor length. The operational magnetic field in the 2 MeV cooler toroids is about 1.0 kG. In order to avoid the heating of electrons passing the toroids, the longitudinal magnetic field should be adjusted for different electron energies to get a suitable Larmor length value [5].

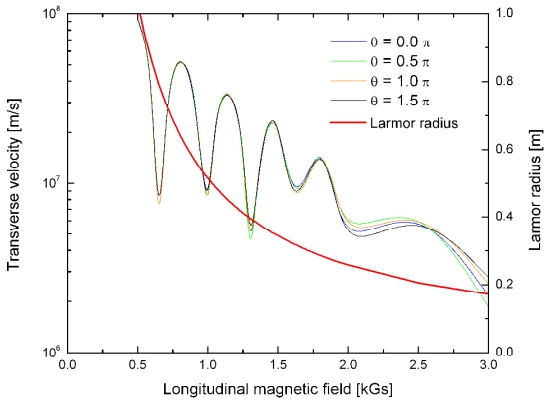

Fig. 2: dependence of the electron transverse velocity on the longitudinal magnetic field value in toroid.

References:

[1] J.Dietrich et al, RuPAC-10 Proceedings, 2010
[2] J.D.Jackson, Classical Electrodynamics, 1975
[3] V.V.Parkhomchuk, design report of IMP coolers, 1999
[4] M.Nishiura et al, NIMA 532, 2004
[5] M.I.Bryzgunov et al, COOL-09 Proceedings, 2009

Design Simulations for Pellet Tracking Systems

A. Pyszniak[a,b], H. Calén[a], K. Fransson[a] and Z. Rudy[b] for the pellet tracking group

A pellet tracking (PTR) system for PANDA is under development in Uppsala. Tests and measurements at the Uppsala pellet test station (UPTS) are an important component in this work. A system [1] based on two line-scan (LS) cameras and diode lasers has been used during the last years.

The pellets are generated with a constant frequency in the range 40 to 80 kHz. Due to different kinds of losses, the pellet rate at the measurement levels is typically between a few to twenty k pellets/s. Each camera measures the transverse position and time of the pellets. As was shown in Ref. [2], the time spectra are well understood. Making a cut on the time difference between recorded pellets at two measurement levels, one can select measurements from both levels, that with high probability correspond to the same pellet. Then, the information about the measured pellet position is used to extrapolate the pellet track back to the VIC (Vacuum Injection Capillary, nominal pellet generation point).

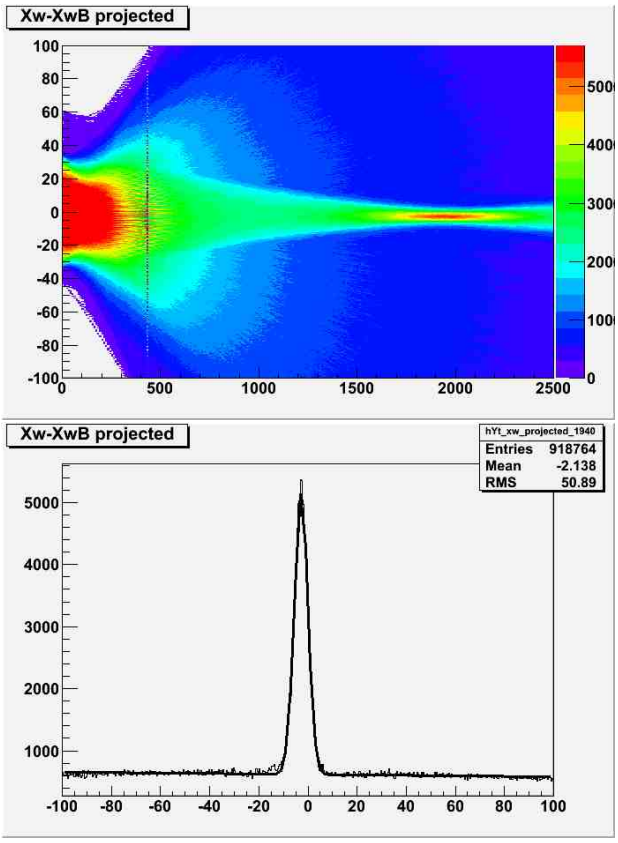

Figure 1. Extrapolated transverse positions of pellet tracks from experimental data taken at UPTS (upper plot), and a slice taken at the nominal position of the VIC exit (lower plot). In the upper plot the scale on the x-axis is in millimeters and on the y-axis in pixels (≈ 37 μm). In the lower plot the scale on the x-axis is in pixels.

The upper plot in Fig. 1 shows the extrapolated transverse position of pellet tracks in the direction of the VIC. Making a slice in the plot at 1940 mm which is the nominal position of the VIC exit (lower plot in Fig. 1), one obtains a resolution of the reconstruction of $\sigma \approx 100$ μm. The measurement levels are at 0 and 427 mm. Taking into account the distance to the measurement levels and the distance between them, the

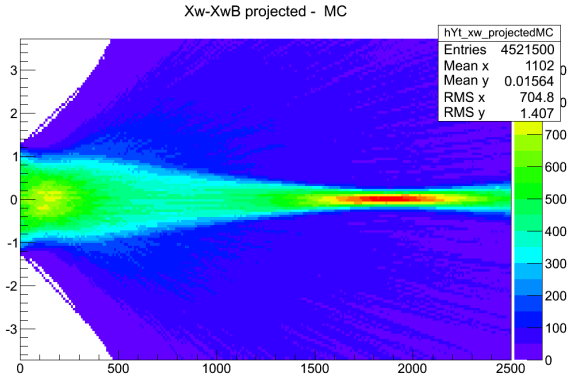

Figure 2. Simulation of pellet tracking at the UPTS (see Fig. 1). The scale on both axes is in millimeters.

detection resolution at the measurement levels is estimated to be ≈ 20 μm. The results of the measurements are well described by the MC simulation (Fig. 2). The deviation from the experiment seen in the left part of the plot is due to background pellets that are not included in the simulation.

The aim of the design simulation studies is to check how the expected position resolution and tracking efficiency for different design variants meets the goals and requirements from the physics experiment and find out how they depend on various parameters describing the pellet and pellet stream properties and the detection process. The geometrical conditions and tracking equipment configurations are based on a conceptual design for PANDA where two 0.4 meter long sections of the vertical pellet beam pipe are reserved for the tracking system, one at the pellet generator and the other one at the dump. At each section four measurement levels can be accommodated.

In the design simulations we calculate the true position and time of each pellet at the measurement levels. This information is then used to simulate the measurements of pellet position and time. The simulation takes into account various aspects of the measurement, as illumination, optical imperfections and electronics noise. Parameters in the simulations are the pellet physical size, camera pixels size and structure of the camera cycle (period and exposure time). Based on the experimental results from the UPTS, we simulate the pellet brightness using a realistic distribution.

Due to various optical effects, like the effect of the depth of field or optical aberrations, pellets may appear bigger, than they are in reality. Also, the position of the pellet center of brightness, measured by the experiment, may differ from the position of the center of mass. These two optical effects are taken into account. To estimate the amount of light collected by a camera pixel we first measure the integrated amount of light. Here we take into account the pellet brightness, time of flight in front of the camera, pellet and camera sensor overlap and camera dead time. The light is divided between every pixel which saw the pellet, according to their overlap. Also, the signal noise in pixels is taken into consideration. We can also put thresholds on the minimum amount of light in a single pixel and in the whole cluster. The pellet position is cal-

culated as a weighted average of positions of pixels, with amount of collected light as the weight. The measured time is taken as the middle of the exposure time of the cycle.
During the pellet tracking procedure we take each pellet recorded at the first measurement level as a start and for this pellet we want to collect all information needed to reconstruct the time and position of this pellet at the interaction region. To reconstruct the track of the pellet we need to know the position of the pellet at the following measurement points. To select the correct measurement from among all others, we use the mean velocity of the pellet stream and distance to the second measurement level, to get the expected pellet time. We look for measurements around this time, in a certain time window, and the measurement closest to the expected time is assumed to be the measurement of the pellet in the track. Its time is used to calculate a new, improved velocity, which is then used to search for the pellet at the next measurement levels. This is continued until the last measurement level. The whole procedure is repeated for all pellets recorded at the first measurement level.
Having information from all measurement levels, one can fit pellet tracks. The pellet start position (VIC exit) may also be used as an additional point in the track fitting.
One can obtain the tracking resolution in the simulations, by comparing reconstructed and true pellet position at the interaction region. Example resolution plots are shown in Fig. 3.

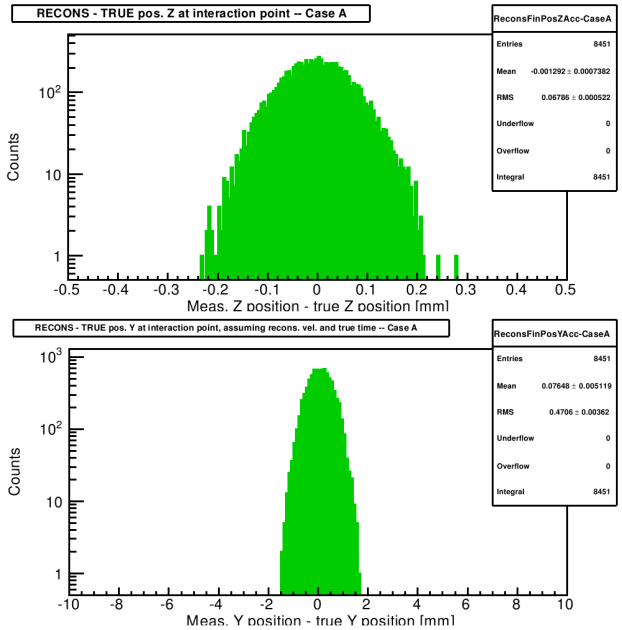

Figure 3. Examples of pellet position resolution from tracking. The upper plot is for the Z (horizontal) coordinate and the lower plot is for the Y (vertical) coordinate.

The resolution in the X and Z directions depends directly on the position measurement resolution and on the distance between the measurement levels. A resolution of $\sigma \approx 250\ \mu m$ is obtained when using information from the upper tracking section only. The resolution is good enough for accurate consistency checking if a track could originate from the VIC exit (situated about 700 mm above the tracking section). If this is the case the pellet stream position at the VIC can be used as an additional point on the track fit, substantially increasing the lever arm. Then a position resolution of $\sigma \approx 70\ \mu m$ at the interaction region is obtained. For the reference conditions, the resolution in the Y direction depends mainly on the accuracy in the velocity determination i.e. on the time resolution from the cameras and the distance between first and last level in the measurement section. The additional measurement levels in between, improve the resolution slightly (≈ 30 %) and results in a resolution of $\sigma \approx 0.8$ mm.
The lower tracking section at the dump might improve the resolution and can also be used for tuning and monitoring of the tracking performance.
The tracking system should provide useful i.e. correct tracking information for as many as possible of hadronic events (taken as the time when there are pellets in the beam region). To evaluate the performance one compares the position and time information for the true pellets with position and time information from the tracks that are reconstructed from the pellet measurements. For a certain target situation i.e. a certain number of pellets present in the interaction region, the efficiency is defined as the probability that the number of pellets found by the tracking is the right number. The correctness can similarly be defined as the probability that the number of pellets expected from the tracking system is the correct number.
From the results of these studies one can deduce that for the reference conditions about 70% of the hadronic events would have correct information from the tracking system and for about 50% of the events there would be unambiguous position information.

The project is supported by COSY-FFE, EC FP7, Swedish Research Council and Foundation for Polish Science (MPD program).

References

[1] H. Calén, K. Fransson, P. Marciniewski and A Pyszniak, IKP Annual report, 2011.
[2] A Pyszniak, H. Calén, K. Fransson, M. Jacewicz and Z. Rudy, IKP Annual report, 2011.

[a] Department of Physics and Astronomy, Uppsala University, SE-75120, Uppsala, Sweden
[b] Institute of Physics, Jagiellonian University, PL-30-059 Cracow, Poland

Development of a Readout and Test System for the Forward Strip Part of the Micro Vertex Detector of $\bar{\text{P}}$ANDA

D. Deermann

The $\bar{\text{P}}$ANDA Micro Vertex Detector will be a combined system of silicon pixel and strip detectors. It will have four barrel layers, with pixel detectors in the inner two layers and strip detectors in the outer two layers.
Furthermore, $\bar{\text{P}}$ANDA has fixed target kinematics and a corresponding boost in forward direction for any reaction. Therefore, six detector discs in the forward direction are implemented in addition to the barrel layers. The first four discs consist of pixel detectors only, while discs 5 and 6 consist of an inner pixel disc together with a surrounding ring of strip detectors. Those rings consist of 24 trapezoidal strip detectors with a stereo angle of $15°$. The trapezoidal sensors are designed and ordered from CiS[1]. Figure 1 shows a sketch of the trapezoidal sensors.

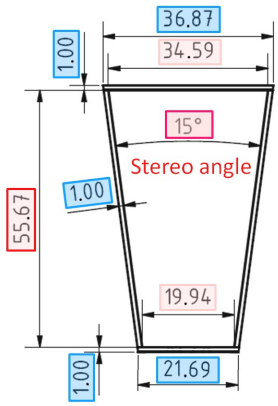

Fig. 1: Trapezoidal sensor geometry, sizes in mm [1].

They are double sided with 512 strips per sensor side. The strips are aligned parallel to the long edges, and therefore have a stereo angle of $15°$ between front and back side strips. The sensors bulk material is n^--doped with p^+-doped strips on the front side and n^+-doped strips on the back side. The depletion of the sensor is realized by connecting a high voltage between the bias-ring (front side) and bulk of the sensor.

To prevent cross talk between the p-side strips the *punch-through* method is used to contact the p^+-strips to the depletion voltage. That means that there is a small n^--doped region between the p^+-strips and the bias ring. In this way, a small initial voltage $U_{init.}$ must be applied to make the depletion zone, that is originating from the bias ring, grow and touch the p^+-strip's depletion zone. The p^+-strip's potential then is $U - U_{init.}$. Isolation between the n-side strips is obtained by p-doping the area between two n-doped strips, this method is called *p-spray*.

To assure the sensors quality it is important to determine their depletion voltage and leakage current. A test system to measure IV and IC curves, as well as single and multiple strip capacitances, has been set up. From those measurements all important values can be obtained. The test system is composed of a semiautomatic Probestation table, a high precision LCR[2] meter, a high voltage supply, and a PC and software that is programmed to control the voltage supply and LCR meter. With the software it is possible to automatically run through different bias voltages and measure the corresponding sensor capacitance and leakage current. After the sensor's quality has been assured by characterizing its electrical properties, it can be installed in a readout system.

A readout system is available for the rectangular pixel and strip sensors and will be adapted for the trapezoidal sensors. The pixel sensors are bump bonded on a sensor board that is connected to a ML605 [2]. The ML605 is a FPGA[3]-based data acquisition board with LAN connection to a PC.
The ML605 readout system was developed at IKP-1 and will also be used for the trapezoidal sensors. However, the trapezoidal sensors are strip sensors and use an APV25 frontend chip instead of the ToPix frontend, which is designed for pixel sensors. Therefore, some requirements of the readout system have to be adjusted. The APV25 was first developed for CMS[4]. Although the rectangular strip sensors run with the same technology as the trapezoidal sensors, their geometry differs. A trapezoidal sensor board needs a geometry suited to their shape and the same electrical characteristics as the rectangular sensor board [3], which was developed in the HISKP of the University of Bonn.

The sensors will be fixed on the sensor board and wire bonded to the APV25 frontend chips. Each APV25 can handle 128 channels, which means that we need four APV25s for the 512 channels per sensor side. The sensor is operated with high voltage so that the front and back sides of the sensor are at a different potential. Therefore, the corresponding frontend chips from the front and back sides of the sensor board need to be operated on a different ground level. Thus, the front and back sides of the board must be galvanically separated. All supply voltages for the APV25s and the sensor, as well as the signal lines, will be gathered and distributed on a supply board. Since the signals from the front and back sides of the sensor board come with different ground potentials, this supply board also needs two galvanically seperated regions for connecting these signals. The signals coming from the back side of the sensor board will be transformed to front side potential, so that all signals can be forwarded to the same readout system without a potential difference between the signal lines. The supply board was developed in the HISKP of the University of Bonn.

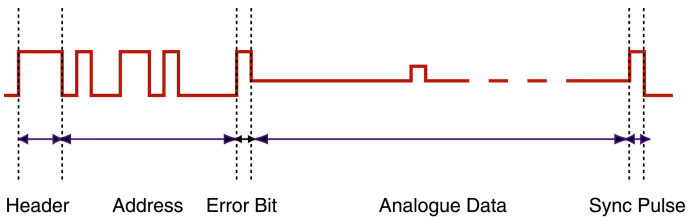

Fig. 2: Output scheme of the APV25 frontend chip [4].

In contrast to the ToPix, the APV25 does not digitize the channels but forwards an amplified analog signal. The output scheme can be seen in Figure 2. Thus, the task of digitization has to be performed by the further readout system. This task will be handled by a Nutaq MI125 ADC[5] card. It has 16

[1] Forschungsinstitut für Mikrosensorik und Photovoltaik GmbH
[2] Inductance (**L**), Capacitance (**C**), and Resistance (**R**)
[3] **F**ield **P**rogrammable **G**ate **A**rray
[4] **C**ompact **M**uon **S**olenoid, a detector at the LHC, CERN
[5] **A**nalog-to-**D**igital-**C**onverter

channels so that 16 APV25s can be connected, which means the signals of 2 sensors with 8 APV25s per sensor can be digitized by one MI125 card. Figure 3 shows a sketch of the complete setup. As mentioned, this sketch can be upgraded

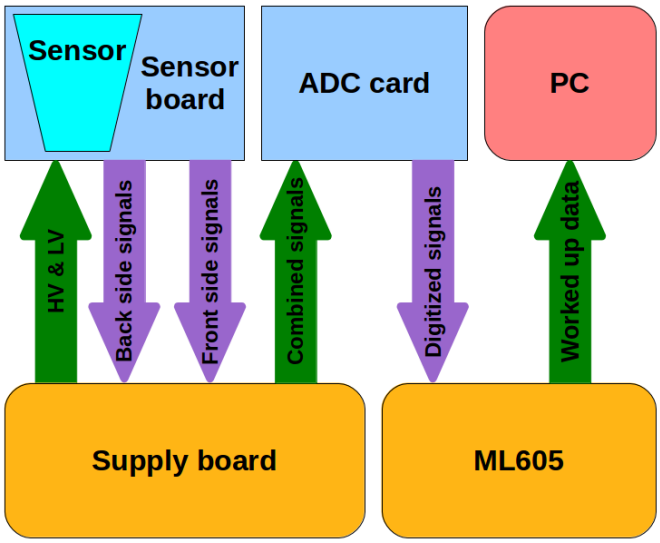

Fig. 3: Sketch of the complete readout system.

by connecting two sensor boards and two supply boards to one ADC card.

In addition to these hardware changes, the firmware for the Virtex 6[6] has to be extended to work with the APV25's output. The most basic change will be adjusting the readout format according to the different output schemes of the ToPix and APV25 frontend chips. Due to higher noise in strip sensors compared to pixel sensors, an online calibration for the baseline and pedestal movement has to be implemented as well.

References:

[1] Design optimization of the PANDA Micro-Vertex-Detector for high performance spectroscopy in the charm quark sector, Ph. D., Thomas Würschig, University of Bonn, 2011

[2] The Jülich Digital Readout System for PANDA Developments, Simone Esch, IKP-1, DPG Frühjahrstagung 2012

[3] Entwicklung von Testsystemen zur Charakterisierung von Silizium-Streifen-Detektoren, Diploma Thesis, Sebastian Krah, University of Bonn 2012

[4] APV25-S1 User Guide Version 2.2, Lawrence Jones RAL Microelectronics Design Group

[6] Virtex 6 is the name of the FPGA used on the ML605

Development of Front End Electronics for the PANDA Straw Tube Tracker (STT)

A. Erven[1], W. Erven[1], P. Kulessa[1,2], B. Lorentz[1], M. Mertens[1], R. Nellen[1], H. Ohm[1], D. Prasuhn[1], T. Preuhs[1], K. Pysz[1,2], J. Ritman[1], V. Serdyuk[1], P. Wintz[1], P. Wuestner[1]

The central Straw Tube Tracker (STT) in the PANDA target spectrometer has to measure both the helical trajectories of charged particles with a spatial resolution of about 150 μm and the specific ionization energy-loss (dE/dx) for an identification of the particle species in the momentum range below about 1 MeV/c. An accuracy of better than 10% for the dE/dx measurement is required for a sufficient separation of protons, pions, and kaons in the lower momentum region.
Earlier straw prototype tests have demonstrated an achievable spatial track resolution of better than 150 μm. [1]. In addition, a resolution of the specific energy-loss (dE/dx) of about 8 % has been measured with a multilayer straw detector with 20 hit straw tubes per track [1, 2].
Currently, the activities aim at the development and commissioning of the frontend readout electronics for the PANDA-STT. The signal readout system must assure the simultaneous and precise measurement of drift time and energy-loss at high particle rates in the straw tubes of up to 1 MHz/cm^2 which corresponds to a beam-target luminosity at PANDA of 2×10^{32}/cm^2/s. Also the severe environmental conditions in the PANDA Target Spectrometer, like space occupancy, heat management with low power consumption and lowest electromagnetic noise pickup have to be fulfilled.

Two alternative readout systems for the PANDA-STT are currently under consideration:
A specific, programmable readout chip (ASIC) featuring ion tail cancellation and a baseline restoration at highest signal rates is being developed. The ASIC measures the leading edge and the Time-over-Threshold (TOT) of the analog signal shape with a resolution of about 1 ns. The drift time is deduced from the leading edge time and the energy-loss from the Time over Threshold (ToT) information. The ASIC development is a common effort by the PANDA groups from the AGH University and the Jagiellonian University, both from Kraków, Poland.
Another readout system consists of a discrete electronic chain comprising a signal booster frontend at the STT and a shaping amplifier coupled to an FPGA-FADC readout, both located outside the detection system. This readout system is developed by IFJ PAN in Kraków (Poland) and the IKP and ZEL at FZ Juelich. The signal booster is a 16-channel charge sensitive preamplifier with the input impedance adjusted to the straw impedance. It contains an integration amplifier and voltage amplifier (gain factor 4). The 16-channel shaping amplifier consists of:

- differential input amplifier (gain 1.4)
- signal tail cancellation
- three integration stages
- baseline restoration circuit at the last integration stage

The total gain of each channel is 2.3 mV/fC whereas the predicted noise level (peak-to-peak) is 2 fC. Intermediate signal transmission can be done via coaxial or twisted-pair cable with a length of about 5 m. The time and energy information are derived from a signal shape analysis of the recorded FADC data done in realtime by a FPGA. The readout circuit features an ion tail cancellation and baseline restoration up to a signal rate of more than 2 MHz per channel.

Two straw prototypes equipped with the two different readout systems have been tested with the COSY proton beam at low (up to 100 kHz/cm^2) and high (up to 2 MHz/cm^2) intensities. During 5 days three different beam momenta were selected (2.0, 0.9 and 0.6 GeV/c) to investigate the different ionization energy-losses of the proton particles in the straws. The first straw setup was readout by a 32-channels frontend ASIC board, followed by a Time Readout Board (TRB). The second straw prototype was equipped with eight 16-channel signal boosters coupled to appropriate shaping amplifiers and followed by FADC readout. In this case the data were collected with the use of the standard Juelich DAQ.

In the following the results of the second readout system (FADC) are described. The analysis of the data taken with the ASIC+TRB readout system in December 2012, are still ongoing.
In order to find the proper integration time for the analog straw signal with respect to both, time and integrated charge resolution, readout boards with 5 different integration constants have been designed for a direct comparison: 6, 15, 33, 73, and 165 ns.
The data analysis includes a calibration of the drift time to isochrone radius relation, a hit selection and track reconstruction algorithms. Fig. 1 shows the obtained spatial and energy resolution of reconstructed proton tracks. As can be seen, for integration times of 40-60 ns the time and energy resolutions match the requirements for the final PANDA-STT with about 150 μm spatial and better than 10% energy-loss resolution.

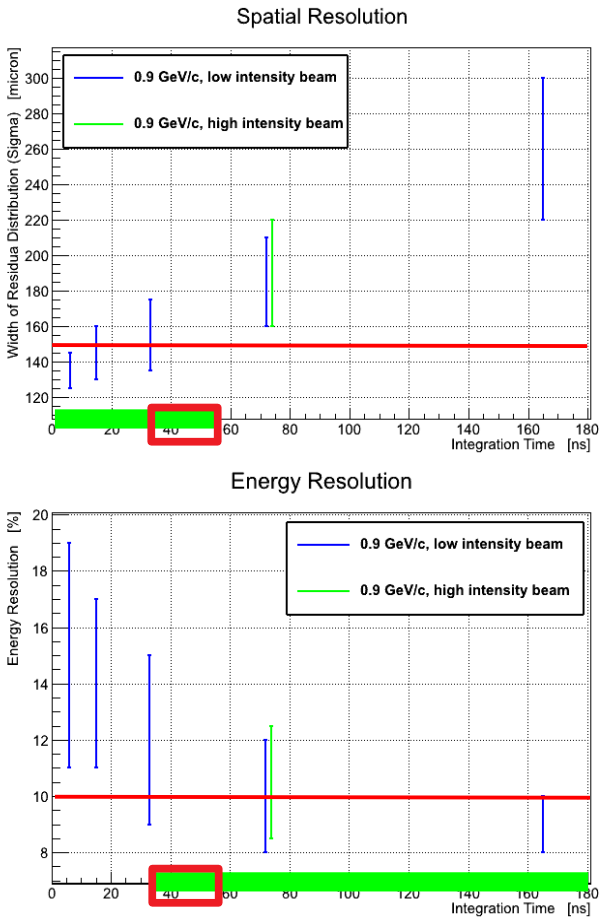

Figure 1: Spatial (top) and energy (bottom) resolution measured with a straw prototype in a proton beam of 0.9 GeV/c momentum. The straws are readout by FADC. The red lines indicate the required resolutions for the PANDA-STT. The read boxes mark the region of the proper amplifier integration times.

A high spatial straw resolution requires rather short integration times whereas a high energy resolution needs longer integration times. The test results demonstrate for the first time a sufficient resolution of both space and energy measurement with the same common readout system.

[1] Technical Design Report of PANDA Straw Tube Tracker, *http://arxiv.org/abs/1205.5441v2*
[2] S. Costanza et al., IKP-COSY Annual Report 2011.

[1] FZ Juelich, [2] IFJ PAN Kraków

This work was partially supported by the FFE program of JCHP-FZJ.

Upgrade of the Jülich Digital Readout System for the $\overline{\text{P}}$ANDA-MVD

S. Esch, T. Stockmanns and J. Ritman for the $\overline{\text{P}}$ANDA collaboration

In order to develop the Micro Vertex Detector (MVD), it is very important to evaluate prototypes and detector components. Different prototypes of the pixel front-end chip ToPix (Torino Pixel) need to be tested and characterized under similar conditions to further the development. To control these devices under test (DUT) and to save the collected data a suitable readout system is necessary. It is regular to have similar conditions for the different prototypes and development stages thus a modular concept of the readout system is required which can be simply adapted to the specific interface of electronics. At the same time the system must provide a high performance to allow the evaluation of single front-end chips as well as fully assembled modules.

To meet the requirements of an upcoming full size ToPix prototype and online analysis, an upgrade of the Jülich Digital Readout board and the readout firmware was developed [Mer10].

The Jülich Readout System is a compact and powerful table top setup which allows a quick testing of new detector components.

The central component is the FPGA (Field Programmable Gate Array) based readout board (see Figure 1). It is connected to the readout PC via an optical connection which is used to receive commands from the user and to send data to the PC for further processing. The corresponding software infrastructure is implemented within the MVD readout framework (MRF). The prototype is controlled by the user with a graphical user interface (GUI). On the other side the readout board is connected to the DUT on its test board. An intermediate adapter board converts the DUT signal interface to the interface of the readout board. The ML605 evaluation board (see Figure 2) is taken as the digital readout board for the system. It is a commercial product of Xilinx and is comparatively cheap and easy to obtain. It contains a DDR3 RAM slot for data storage and a Virtex 6 FPGA. The connection to the PC is established via a SFP gigabit transceiver.

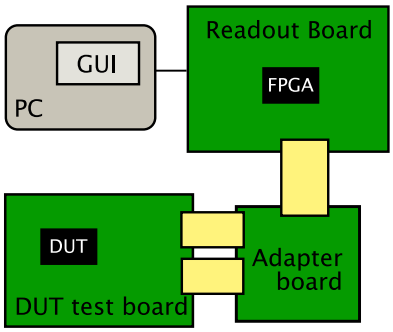

Fig. 1: Schematic drawing of the Jülich Readout System for ToPix 2 measurements.

The FPGA on the digital readout board is configured with a firmware which implements the desired functionality and configures the external interfaces. The firmware for the readout board is written in VHDL, a hardware description language, and then synthesised with the Xilinx development tools, i.e. translated to a format which is understandable by the FPGA. The firmware is divided into modules which handle different subtasks concerning the DUT, the board functionality or the communication. All modules are connected to the register manager which is itself connected to the SIS1100 interface (see Figure 3).

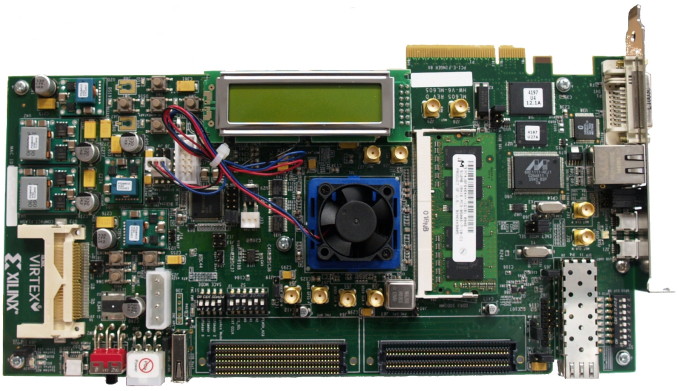

Fig. 2: The digital readout board ML605 from Xilinx with a Virtex 6 (middle, underneath fan), SFP port (lower right), FMC connectors to adapter board (lower center), Compact Flash slot (left) and DDR3 RAM (next to FPGA on the right).

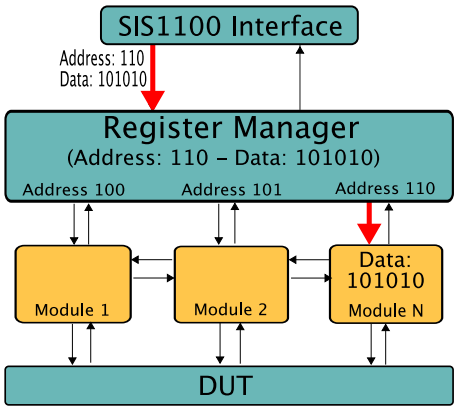

Fig. 3: Schematic firmware setup. Data delivered via SIS1100 will be distributed to the modules indicated by the address. The red arrows indicate the path of the shown example data packet.

Data which arrive via the SIS1100 are formatted in address-data pairs. The register manager will distribute the data depending on the address to the concerning modules. If data should be read from the board, the register manager will take the data from the module indicated by its address. This modular design makes it easy to adapt the firmware to a different readout board or a different DUT respectively.

The readout system was adapted to read out the recent front end prototype for the pixel detector of the MVD, ToPix3. The ToPix ASIC uses the time-over-threshold (TOT) method to measure the deposited charge. Different measurements for the calibration, functionality testing and performance have been performed.

One important calibration step is the tuning of the pixel thresholds to the same value. Due to variations of the production process the effective threshold of different pixels can

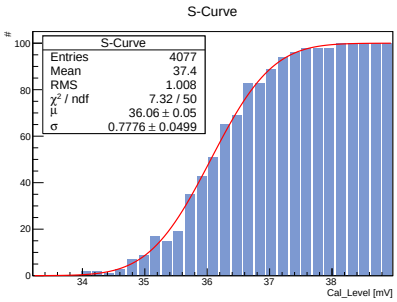

Fig. 4: Determination of the threshold for a single pixel with the internal injection circuit. The blue curve describes the response of the pixel as a function of injected charge. The red curve is a fit with an error function (from [S. 13]).

vary even if they are set to the same nominal setting. This demands that a higher global threshold setting must be used in order to suppress noise hits, however, this reduces the signal amplitude and the sensitivity for small charge deposits in the detector. Therefore the ToPix each pixel's threshold can be calibrated with a 5-bit DAC. In Figure 4, the method to define the threshold is shown. Charge has been injected into the pixel with the internal injection circuit around the defined threshold. The ideal behavior would be a step-function. Due to noise, the step-function is broadened and gets its characteristic S-curve shape. The width of the S-curve is a measurement for the noise of the pixel, the midpoint defines the actual threshold. The measurement shows the expected S-curve response of the pixel. In Figure 5 the threshold distribution of all pixel is shown before (black) and after (blue) the tuning of the thresholds. One can see the narrowing of the distribution after the tuning.

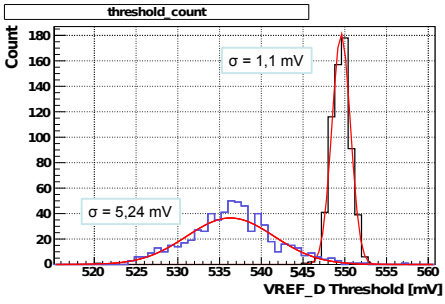

Fig. 5: Tuning of the single pixel threshold for a ToPix3 module. Blue curve: Threshold distribution before tuning. Black curve: threshold distribution after tuning. Red curves: Gaussian fits (from [S. 13]).

A readout system has been set up to control and characterize front-end ASICs for particle physics experiments. An interface for the recent $\overline{\text{P}}$ANDA MVD ASIC, ToPix 3 has been added to the readout system. Measurements of the central characteristics of the front-end ASIC has been performed and matches the expectations. Further measurements are ongoing. The next prototype ASIC ToPix 4 will also be integrated in the readout system upon its arrival next year.

References:

[Mer10] Marius C. Mertens. *Der Panda Mikro Vertex Detektor: Endwicklung eines Labormessystems, Simulation der MVD-Betriebsparameter sowie Untersuchung zur Auflösung der Breite des $D^*_{s0}(2317)$.* PhD thesis, Ruhr-Universität Bochum, 2010.

[S. 13] S. Esch, W.Erven, M.C. Mertens M.Ramm, J.Ritman and T.Stockmanns. Development of a readout system for the PANDA Micro Vertex Detector. *JINST 8*, (C01043), 2013.

Implementing an Ethernet Communication Module Based on the UDP Standard into the Jülich Digital Readout System

A. Goerres

The $\overline{\text{P}}$ANDA[1] experiment is one of the main experiments at the FAIR[2] facility, which is under construction in Darmstadt. It consists of several components, where the Micro Vertex Detector (MVD) is the innermost part. Because $\overline{\text{P}}$ANDA features a new concept with a trigger-less readout, existing electronics cannot be used for the readout of sensors.
The Jülich Digital Readout System (JDRS) is a setup to test these new readout chips. It was developed for the MVD pixel front-end electronics, but is designed in a modular way, which is easily adapted to other needs. A communication link between the electronics under development and a readout PC has been implemented to make it even more convenient to use. It is based on a gigabit Ethernet connection using copper cables and the UDP standard.

The concept of the Jülich Digital Readout System The JDRS was developed to set up a flexible test system for front-end chips under development. It is based on a commercially available development board, the ML605 from Xilinx, featuring a Virtex 6 FPGA[3]. On this FPGA the JDRS firmware handles the interaction between the attached front-end chip and a software running on a connected readout PC. This software includes a modular framework, the MRF[4], which is structured in abstraction layers.

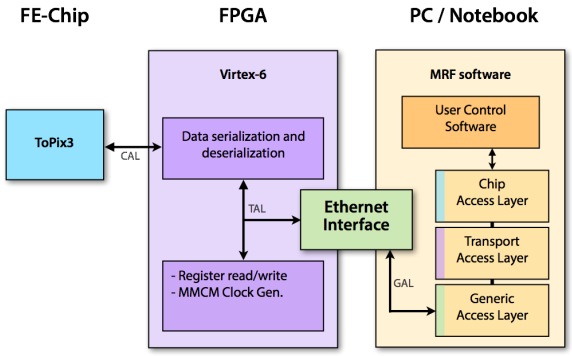

Fig. 1: The Schematic Data Flow Inside the JDRS.

In figure 1 the different components and layers of the system are shown: The Chip Access Layer (CAL) deals with the data structure of the chip, the TAL[5] corresponds to the structure needed by the readout board and the GAL[6] handles the basic communication requirements. A more detailed description of the system is given in [1].

The User Datagram Protocol (UDP) The last level, the basic communication, is implemented with an UDP module, which allows the utilization of highly available Ethernet hardware. UDP is a way of structuring data that is transferred over an Ethernet connection. An UDP packet starts with several blocks of information like the destination and source addresses, the protocol type, a checksum for the header, and the length the header and payload. After that follows the payload data with a length up to 1472 bytes.

Adjusting the module to the existing setup Because the JDRS is already in use with another communication system[7], the implementation of the Ethernet module should leave other components of the firmware untouched as far as possible. That produces some requirements to the UDP payload data structure as well as the handling of the data inside the firm- and software. For instance, the transferred data is split into 32 bit blocks[8] and the first transferred block defines, which action is requested.

Possible performance To use the UDP connection in a reasonable way, it has to fulfill not only structural features of the current communication but it should also match the needs of the front-end electronics under development. For the MVD that means it should be able to deal with data rates in the order of 600 MBits/s [2].

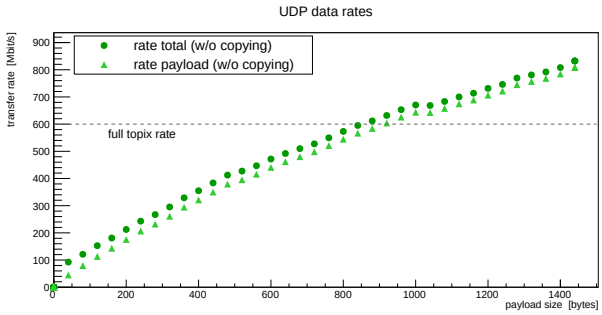

Fig. 2: Achieved Data Rates Between PC and Readout Board via UDP.

As an early check, possible data rates between a PC and the readout board were measured. For increasing sizes of random payload data the achieved rates can be seen in figure 2. Payload sizes larger than roughly 2/3 of the maximum exceeds the requirement for the maximum expected data rate (dashed line). Thus a testing environment can be established, which is able to simulate future operation.

Outlook After including all the needed features into the UDP implementation, a detailed testing against possible errors during operations is necessary. Moreover a benchmark transferring real data has to be done.

References:

[1] Der PANDA Mikro Vertex Detektor: Entwicklung eines Labormesssystems, Simulation der MVD-Betriebsparameter sowie Untersuchungen zur Auflösung der Breite des D*. Ruhr Universität Bochum. PhD Thesis. Marius C. Mertens (2010).

[2] Technical Design Report for the: PANDA Micro Vertex Detector. PANDA Collaboration (2012). http://panda-wiki.gsi.de/pub/Mvd/MvdTalkOrPaperDrafts/panda_tdr_mvd.pdf

[1] Anti-**P**roton **An**nihilation at **Da**rmstadt
[2] **F**acility for **A**ntiproton and **I**on **R**esearch
[3] **F**ield **P**rogrammable **G**ate **A**rray
[4] **M**VD **R**eadout **F**ramework
[5] **T**ransport **A**ccess **L**ayer
[6] **G**eneric **A**ccess **L**ayer

[7] The current communication is done via the SIS1100 standard, a development with the ZEL of Forschungszentrum Jülich.
[8] This correlates to the transferred block size of the SIS1100 protocol.

Implementations of Hough Transformations on GPUs for PANDA

A. Herten

The $\overline{\text{P}}$ANDA[1] experiment is one of the main experiments of the upcoming FAIR[2] facility that is under construction in Darmstadt. The planned event rate is $2 \cdot 10^7$ /s. Because background and signal events have similar signatures in the energy region to be investigated, a hardware-level trigger is not foreseen for the experiment. Instead, fast online event reconstruction will substitute for this element. The full event rate leads to a data rate of approximately 200 GB/s. For further in-depth offline analysis, the online event reconstruction has to reduce this data rate by three orders of magnitude. In current experiments, the reduction is usually executed by an array of FPGAs[3]. For $\overline{\text{P}}$ANDA, the feasibility of GPUs[4] for this task is investigated.
This report presents central principles of this investigation as well as the status of the study.

Tracking A key aspect of particle tracking is to generate continuous, parameterized tracks from discrete hit points of one or more sub detectors. These tracks provide insight into the nature and properties of the recorded particles, which, in turn, are the basis for the decision whether to keep the recorded data or disregard them.

Hough Transformation An algorithm fulfilling the aforementioned properties is the Hough Transformation (HT). It was invented as a bubble chamber image analysis tool by P. Hough [1] and generalized by Duda and Hart [2]. In its basic formulation, the HT's purpose is to extract straight lines from images in an automated fashion.
The HT generates an arbitrary number of lines for each given hit point. Lines are produced with parameters α, the angle between the normal of the generated line and the y axis, and ρ, the smallest distance between the line and the origin, according to this equation:

$$\rho = x\cos(\alpha) + y\sin(\alpha). \tag{1}$$

x and y are the coordinates of the hit point, α is incremented from 0° to 180° with chosen granularity (representing the resolution of the method). Every combination of α and ρ is noted for every hit point. A characteristic picture of this α ρ HT parameter space is obtained (Figure 1), in which the overlapping point ($\alpha \approx 130^\circ$) represents the parameters of the track connecting all analyzed hit points.

GPU Implementation Figure 1 shows is a Hough Transform that is implemented on the GPU. The implementation is done with the Thrust framework [3], a template-oriented library expanding Nvidia's CUDA C/C++. Thrust mimics the widely used C++ Standard Template Library (STL) and gives implementations and expansions specifically for GPUs. The result is a well-structured code that uses fast pre-programmed core procedures for computations; the entire process of generating CUDA kernels is shielded from the user by a layer of abstraction.

[1] Anti-Proton Annihilation at Darmstadt
[2] Facility for Antiproton and Ion Research in Europe
[3] Field Programmable Gate Array
[4] Graphics Processing Units

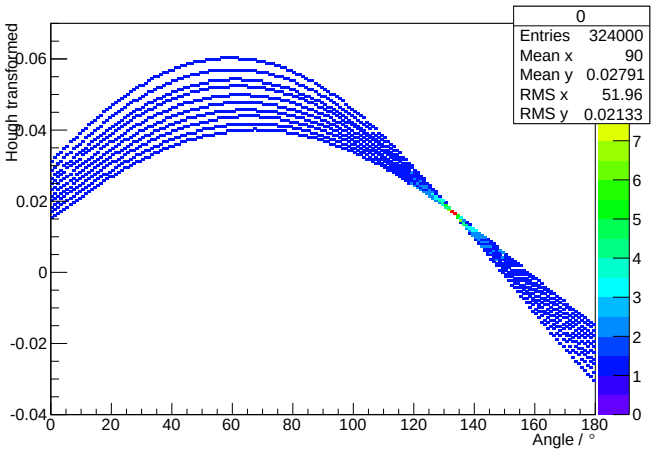

Fig. 1: Parameter space distribution of a Hough Transformation of 10 hits.

On the downside of this Thrust approach is the inflexibility when designing kernels. Though many GPU programming tasks can be broken down to the usage of Thrust methods, complicated computations need the full power of plain CUDA code. Taking this into consideration, additionally to using Thrust libraries, the HT is also implemented in plain CUDA. Both realizations are updated synchronously.

Conformal Mapping To extract particle features, tracks in the inner sub detectors of $\overline{\text{P}}$ANDA are bent by a magnetic field, resulting in helix-shaped tracks. The basic formulation of the HT is not capable of finding curved shapes. To reduce the complexity from curve to straight line, a translation step has to be applied before invoking the HT.
For every hit point (x,y) of a track from the origin the Conformal Mapping (CM) generates a new coordinate (x^*,y^*) in the conformal space according to the equations:

$$x^* = \frac{x}{x^2+y^2} \tag{2}$$

$$y^* = \frac{-y}{x^2+y^2}. \tag{3}$$

This transformation maps a circle in (x,y) space into a straight line in (x^*,y^*) space and a HT can again be used.

Computation Times Figure 2 indicates different computation times for the whole CM+HT calculation chain for hits of the $\overline{\text{P}}$ANDA STT done with the Thrust code. Different number of events as well as different resolutions of the HT were investigated. Using 1000 events and the highest HT resolution (720 α steps in the range of 0° to 360°[5]), less than 2 ms computation time per event was achieved on a Tesla K20X GPU card (floating point precision). A peak finding algorithm in the HT has not yet been used.

[5] Using hit points with isochrone information of the STT requires the α parameter space to range to 360°.

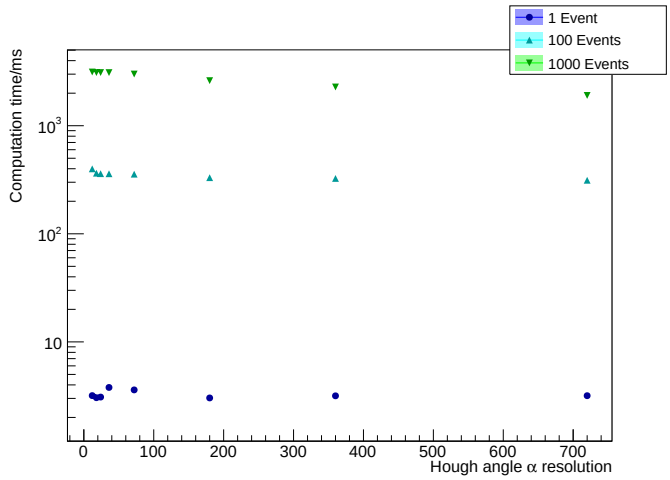

Fig. 2: Computation times for the Hough Transform, including Conformal Mapping, for different number of events (1, 100, 1000) and resolution of the HT.

Outlook In the future, we plan to improve the two implementations in terms of computation speed and feature set. We will investigate other pre-made HT implementation (together with the FZJ Nvidia Application Lab) and, more generally, port other tracking algorithms onto the GPU.

References:

[1] P. Hough, Machine Analysis of Bubble Chamber Pictures, Proc. Int. Conf. High Energy Accelerators and Instrumentation, 1959

[2] R. O. Duda & P. E. Hart, Use of the Hough Transformation to Detect Lines and Curves in Pictures, Comm. ACM, Vol. 15, pp. 11 – 15 (January, 1972)

[3] J. Hoberock & N. Bell, Thrust, http://thrust.github.com

Si Detector Test for the HESR Day-One Experiment

Qiang Hu[1,2], Huagen Xu[2], James Ritman[2]

The proposed day-one experiment at HESR is a dedicated measurement of antiproton-proton elastic scattering. The aim of the day-one experiment is to determine the elastic differential parameters (total cross section σ_T, the ratio of real to imaginary part of the forward scattering amplitude ρ, and the slope parameter B) by measuring a large range of 4-momentum transfer squared t (0.0008 - 0.1 GeV^2). The conceptual design of the day-one experiment is to measure the elastic scattered antiproton and recoil proton by a tracking detector in the small polar angle range and by an energy detector near 90^o, respectively. The recoil arm covers a maximum polar angle from 71^o to 90^o and consists of two silicon detectors and two germanium detectors. All detectors are single-sided structure with 1.2 mm pitch on the front side. The silicon detectors are 1.0 mm thick with sensitive area 76.8 mm (length)×50.0 mm (width). The dimensions of the germanium detectors are 80.4 mm (length)×50.0 mm (width)× 5.0 mm (thickness) and 80.4 mm (length)×50.0 mm (width)×11.0 mm (thickness), respectively. The silicon detectors will be used to detect recoil protons with energy up to about 12 MeV and the germanium detectors will be used to detect protons with energy from 12 MeV to 60 MeV. Currently, one recoil arm is being constructed and four detectors are available as shown in Fig. 1.

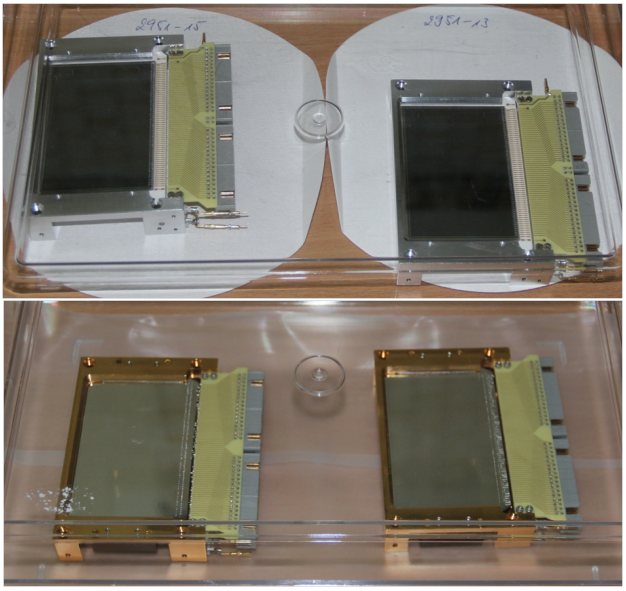

Fig. 1: Photos of Si (upper) and Ge (lower) detectors

Two silicon detectors (Si_#1 and Si_#2) have been tested with a radioactive source (^{244}Cm) in the lab. They were tested at both room temperature (around 300 K) and low temperature (the lowest test temperature for Si_#1 was 124 K and for Si_#2 was 113 K). For both Si_#1 and Si_#2, the energy spectra of all strips on the front side are similar and the two α peaks (5.763 MeV and 5.805 MeV) can be distinguished clearly as shown in the left side of Fig. 2. For the rear side, two-peak like structure can be observed from the energy spectrum as shown in the right side of Fig. 2.

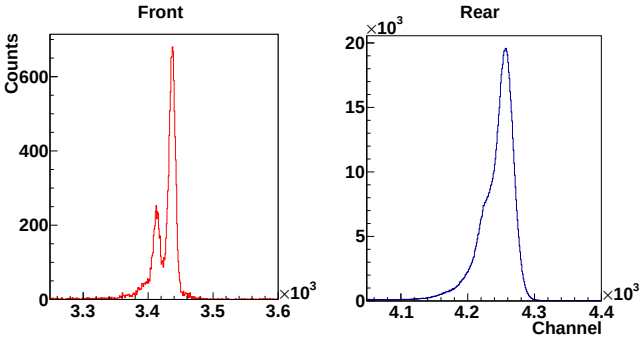

Fig. 2: Energy spectra of one strip on the front (left) and rear side of Si detector (right).

In order to study the performance of these silicon detectors, the energy resolution (FWHM) as a function of bias voltage of each strip has been measured at different temperatures. The energy resolution (FWHM) is shown in Fig. 3 for five example channels. As one can see, the energy resolution of both Si_#1 and Si_#2 shift from 20.0 keV to 26.0 keV at room temperature between 150 V and 200 V. After cooling down, the energy resolution of Si_#1 has improved by about 1 keV and Si_#2 has improved by around 1 to 3 keV.

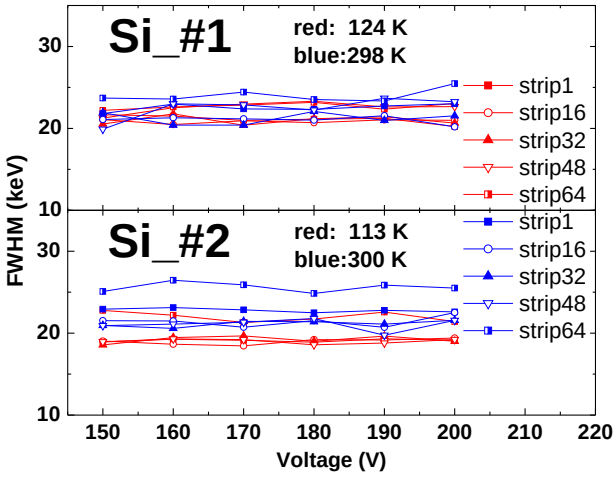

Fig. 3: Plot of energy resolution (FWHM) as a function of bias voltage at different temperatures (blue: room temperature; red: cooling down).

In summary, the test results indicate that the two silicon detectors (Si_#1 and si_#2) are operational and work properly and their energy resolution (FWHM) can be improved a few keV after cooling down compared with that at room temperature.

[1]Institute of Modern Physics, CAS, 730000 Lanzhou, China
[2]Forschungszentrum Juelich, 52425, Germany

Towards the Data Transmission from PandaRoot to the Compute Node

J. Patel, M. Mertens

1 Motivation

The data acquisition of PANDA comprises self-triggered sub-detectors, a global time distribution system, data concentrators and compute nodes. As raw data will be streamed to the DAQ, PANDA will apply online computing techniques in the compute nodes for feature extraction, association of data fragments to the events, event building and finally event selection [1]. The compute nodes will run online reconstruction algorithms programmed in VHDL on FPGAs for data reduction and event selection. This will provide a high flexibility in the choice of the trigger algorithms.
In order to develop the required reconstruction algorithms, simulated data from PandaRoot needs to be transmitted to the compute node. Here we present a module which controls the LEDs on the compute node and can be extended to provide capabilities for data transmission at a later stage.

2 Development

The compute node [2] comprises 5 Xilinx Virtex 4 FX60 FPGAs. Each FPGA features two 300 MHz PowerPC 405 cores. In addition to other peripherals on the PCB, each FPGA is connected to four LEDs on the compute node. The module developed here allows to control these LEDs, i.e. let them blink. The blinking frequency can be controlled by the PC via an RS232 link to the compute node.
On the compute node, this functionality is realized by combining custom logic (LED_Blinker) which controls the LEDs and a program which is executed on the PowerPC to accept the RS232 connection from the computer.
The work can be subdivided into two major parts which have been carried out using the Xilinx EDK design tools:

- Firmware Development
- Software Development

2.1 Firmware Development

We have configured the PowerPC 405 processor available on the FPGAs to include peripherals such as interrupt controller, ethernet MAC, UART lite, GPIO and flash controller. This ensures compatibility with the Giessen group's setup [2] and allows the installation of a similar Linux kernel. The LED_Blinker module is also added to the Power PC as a custom peripheral.

2.1.1 Implementation of the LED_Blinker

The LED_Blinker lets the LEDs blink by turning them on and off upon a clock signal. The clock source is a digital clock manager (DCM) on the FPGA which provides a base clock of 100 MHz. This frequency is strongly reduced by a clock_divider (implemented as a VHDL component) before it is used to turn the LEDs on and off (compare Fig. 1). The clock_divider is realized by counting up to a certain stop value at the frequency of the base clock. Each time the stop value is reached, the counter value is resetted and the output clock signal is inverted.
There is a FIFO available between the PowerPC and the LED_Blinker which accepts 32 bit values from the PowerPC. The value written to this FIFO controls the stop value of the clock_divider.

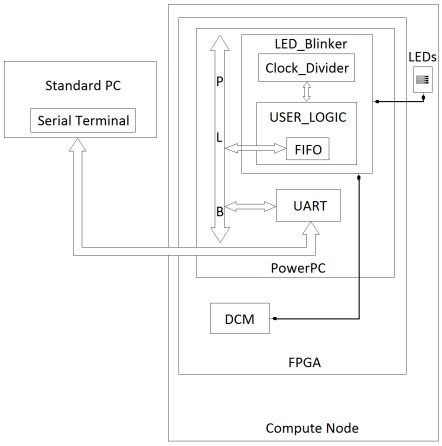

Fig. 1: Data flow from the PC to the compute node controlling the LEDs' blinking frequency. All the components and PowerPC peripherals are shown with their interconnections indicated as arrows.

2.1.2 Configuration of the FPGA

The design is implemented in the Xilinx ISE Project Navigator and the programming file is generated after synthesis and implementation of the source code. The programming file contains all the configuration information which defines the internal logic and interconnections of the FPGA. The generated bit file is downloaded to the FPGA via its JTAG interface using the iMPACT tool.

2.2 Software Development

The hardware design can be exported in order to access the PowerPC's peripherals like UART lite, GPIO, ethernet MAC etc. from the software to be executed on the PowerPC. The purpose of our software is to read it from the PowerPC via UART and write it to the LED_Blinker module in order to set the blinking frequency of the LEDs.

2.2.1 Functionality of C Application

The application uses an RS232 link for the communication between the computer (serial terminal) and the PowerPC. In Fig. 1, the data flow from the serial terminal to the LED_Blinker is illustrated. The data written first goes to the UART via an RS232 link. The Processor Local Bus (PLB) within the PowerPC serves as interconnect between the peripherals . The data from the UART is written on the FIFO via the PLB channel by the program running on the PowerPC. The data written to the FIFO is used to set the stop

value of the clock_divider. In addition, the value of the stop signal is read back via a similar FIFO in opposite direction and sent back to the computer via the serial link to be displayed on the serial terminal.

2.2.2 Execution on the compute node

After successful compilation of the program, the executable file is generated as an ELF (Executable and Linkable Format) binary which runs on the PowerPC. In order to execute the software program on the PowerPC, we need to connect to the PowerPCs debug interface with the computer via JTAG using the XMD console. The ELF file is then downloaded to the PowerPC via this connection and executed afterwards. At this stage one can establish the serial RS232 connection from the computer and set the blinking frequency of the compute node's LEDs. The user input is sent back from the compute node to the serial terminal for verification.

3 Conclusion

We have implemented an LED_Blinker module as the first step towards a data transfer module between the PC and the compute node. We have also developed a software application for the embedded PowerPC which allows for slow control from a PC via RS232. This framework serves as a basis for the implementation of modules for data transfer via ethernet MAC/SFP. The application on the PowerPC can be replaced by a LINUX system for slow control via register access within the embedded PowerPC. The next step is the implementation of further modules which implement algorithms for data analysis on the FPGA.

References:

[1] The PANDA Collaboration, Physics Performance Report for: PANDA (2009)

[2] https://fb07-indico.physik.uni-giessen.de:8443/wiki/index.php/Main_Page [Restricted Access]

Time Resolution of a Flash-ADC System for the $\overline{\text{P}}$ANDA STT

T. Preuhs, W. Erven, A. Gillitzer, P. Kulessa, H. Ohm, K. Pysz, V. Serdyuk, P. Wintz

The required time resolution for the $\overline{\text{P}}$ANDA straw tube tracker (STT) read-out system amounts to approximately 1 ns. One of the potential read-out sytems which fulfills these requirements is the FQDC, a fast charge-to digital converter which samples the signals with a rate of 240 MHz. Realtime analysis in a FPGA[1] permits extraction of timing and charge information. Fitting and interpolation of the data at the signal edge is done in order to overcome limitations of the time resolution due to the sampling period of 4.17 ns. The goal of this work is to measure the time resolution under realistic conditions including long and very thin transfer cables which are expected to modify the shape of detector signals and thus increasing the timing uncertainty.
The FPGA applies two timing methods: The zero-crossing time (t_{ZC}) is defined as the intercept point of the time axis with a straight line fit to the leading edge of the signal. In comparison constant fraction time (t_{CF}) is defined as the interpolation between the two points closest to a predefined fraction of the signal amplitude, as presented below in Figure 1. Direct measurements of the time resolution of the detector system are impractical due to the fact that the time of the appearance of a drift-tube signal is dominated by the drift time. Therefore, signals with a rise time of 2.5 ns and a well defined charge in the range from noise level to about 1 pC are injected into a straw tube with a pulse generator via a small capacitor. For a precise measurement of the contribution of detector, cables and electronics to the time resolution the time difference between double pulses is measured, thus partly cancelling systematical effects of the DAQ.

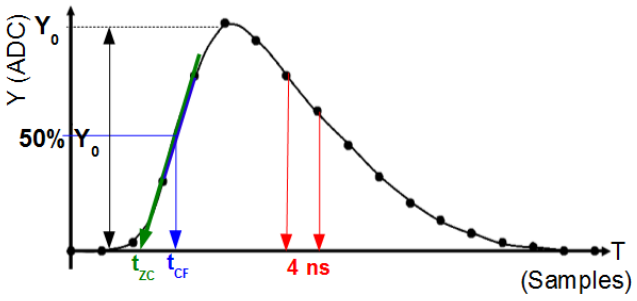

Fig. 1: The derivation of the zero-crossing and constant fraction time.

Experimental Setup Signals from the pulse generator are coupled into a straw tube by a capacitance of 1.2 pF. Behind the straw tube the pulses are transmitted through a thin coax cable with a length of 5 m connecting the straw tube to the preamplifier which is subsequently connected to the FQDC. The described experimental setup is shown in Figure 2. The experimental procedure requires the emulation of double signals with realistic parameters. Therefore, fast double pulses with a rise time of 2.5 ns and an amplitude range from 25 fC up to 720 fC are applied. The standard deviation of the noise is approximately $\sigma = 3.2$ mV.

[1] Field Programmable Gate Arry

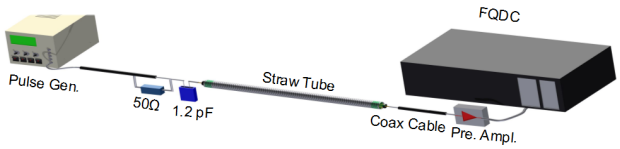

Fig. 2: Experimental Setup.

Time Resolution Measured values of the time resolution (σ) are plotted versus the inverse signal charge in Figure 3. For constant fraction timing all values are below 1 ns, while the zero-crossing technique gives slightly higher values. For a given noise level of the signal baseline and for a fixed signal rise time the time resolution is expected to increase linearly with the inverse signal amplitude (and charge). In the experimental data however, saturation is visible at approx. 0.2 ns. This value is close to the computational accuracy of the FPGA of 0.26 ns and can therefore be considered as a system limit.
The measured time resolution σ_t simply consists in particular of two independent contributions: the noise of the FQDC described by σ_{FQDC} and σ_0 referring to the noise of the experimental setup excluding the Fast QDC. The later contribution is given by the following formula, showing that the deviation of the noise becomes the more relevant the more the signal charge decreases and the more slowly the signal rises, respectively.

$$\sigma_0 = \frac{\sigma_R \cdot \Delta t}{\Delta Q},$$

where σ_R denotes the measured noise of the experimental setup excluding the FQDC, Δt the rise time of the signal and ΔQ the signal amplitude (the signal charge), respectively. Both standard deviations σ_0 and σ_{FQDC} can be linked together to the total standard deviation σ_t by the gaussian error propagation law.

$$\sigma_t = \sqrt{2\left(\frac{\sigma_R \cdot \Delta t}{\Delta Q}\right)^2 + (\sigma_{FQDC})^2}$$

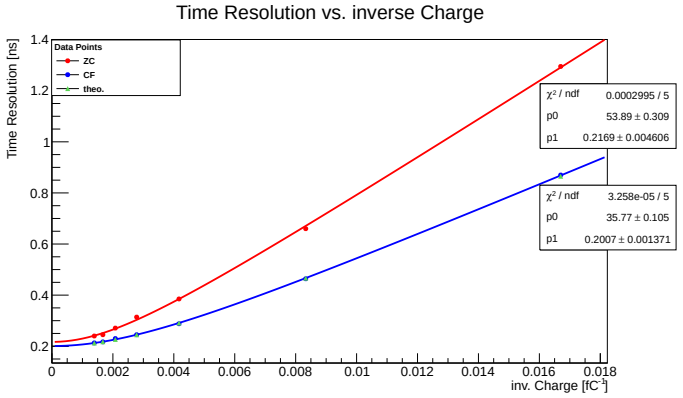

Fig. 3: Measured time resolution as a function of the signal charge. The blue and the red curve are fits to the data for the cf- and the zc timing method, respectively.

For the more precise case of the constant fraction timing method, the measured time resolution is well reconstructed by the formula given above and presented in Figure 3 below by green triangles. For high charge the time resolution has a constant component around $\sigma_t \approx 0.2$ ns and increases proportionally to $1/\Delta Q$ for decreasing charge as described by the formula. This square root function is fitted to the data points for the time resolution σ_t. The blue curve in Figure 3 shows the fit to the data for the constant fraction timing method wheras the red curve in the same figure demonstrates the fit to the data for the zero-crossing timing method, respectively. The constant component results from the time resolution of the FQDC.

Summary and Outlook In this report the contribution of various electronic components to the time resolution was presented. It was determined that a good timing of better than 1 ns can be achieved even for signals with low charge and despite the fact that the FQDC has a sampling period of 4.17 ns, which further qualifies the FQDC as a good candidate for the $\overline{\text{P}}$ANDA STT read-out system. Therefore, the electronic components and in particular the 5 to 10 meter long coax cables do not strongly influence the measured time resolution. This opens up the possibility to transmit the STT signals by thin coax cables out of the inner most detector. The installation of the front-end electronics outside of the detector has two main advantages: the space consuming front-end electronic can be moved outside of the fiducial volume of the detector, and the lower mass budget reduces negative influences on the momentum resolution from e.g. small angle scattering or from converting photons ($\gamma \rightarrow e^- + e^+$). In the future STT signals will be measured with Fe-55- and Sr-90 sources in order to determine the time resolution as a function of the signal charge and width. As a next step, it will be necessary to improve the shielding of the detector to suppress parasitic signals. Furthermore, the impedance must be matched between the straw tube and cable and between the cable and amplifier in order to reduce reflections of the transmitted signals.

References:

[1] W. R. Leo, Techniques for Nuclear and Particle Physics Experiments, Second Revised Edition 1993

[2] Philip R. Bevington, Data Reduction and Error Analysis for the Physical Sciences, 1969

[3] W. Erven, H. Loevenich, P. Marciniewski, P. Wuestner und G. Kemmerling, Berichte zum Datenerfassungssystem fuer physikalische Experimente, Vers. 8, 23. Oktober 2012